Ocean circulation and tropical variability in the coupled model ECHAM5/MPI-OM

J. H. Jungclaus[1], N. Keenlyside[2], M. Botzet[1], H. Haak[1], J.-J. Luo[3], M. Latif[2], J. Marotzke[1], U. Mikolajewicz[1], and E. Roeckner[1]

[1]Max- Planck- Institute for Meteorology
Hamburg, Germany

[2]Leibniz Institut für Meereswissenschaften
Kiel, Germany

[3]Frontier Research Center for Global Change
Yokohama, Japan

Accepted: September 23, 2005

Corresponding author: Dr. Johann Jungclaus
Max- Planck- Institute for Meteorology
Bundesstrasse 53
20146 Hamburg
Germany
Email: jungclaus@dkrz.de

Abstract

This paper describes the mean ocean circulation and the tropical variability simulated by the Max- Planck- Institute for Meteorology (MPI-M) coupled Atmosphere Ocean General Circulation Model (AOGCM). Results are presented from a version of the coupled model that served as a prototype for the Intergovernmental Panel on Climate Change (IPCC) assessment report four (AR4) simulations. The model does not require flux adjustment to maintain a stable climate. A coupled simulation with present-day greenhouse gases is analyzed and the simulation of key oceanic features, such as sea surface temperatures (SST), large-scale circulation, meridional heat and freshwater transports, and sea ice are compared with observations.

A parameterization that accounts for the effect of ocean currents on surface wind stress is implemented in the model. The largest impact of this parameterization is in the tropical Pacific, where the mean state is significantly improved: the strength of the trade winds and the associated equatorial upwelling weaken, and there is a reduction of the model's equatorial cold SST bias by more than 1 K. Equatorial SST variability also becomes more realistic. The strength of the variability is reduced by about 30% in the eastern equatorial Pacific and the extension of SST variability into the warm pool is significantly reduced. The dominant El Niño Southern Oscillation (ENSO) period moves from 3 to 4 years. Without the parameterization an unrealistically strong westward propagation of SST anomalies is simulated. The reasons for the changes in variability are linked to changes in both the mean state and to a reduction in atmospheric sensitivity to SST changes.

1. Introduction

Coupled atmosphere ocean sea ice general circulation models (AOGCMs) have become an important tool for the projection of the Earth’s climate over the next century and beyond. The

ongoing effort of the Intergovernmental Panel on Climate Change (IPCC, 2001) reflects the history and development of the application of coupled models for climate prediction. The IPCC reports also document, however, the diversity of models and the dependence of the findings on the respective models and their parameterizations of sub-grid-scale processes.

The MPI-M atmosphere (ECHAM) and ocean (MPI-OM) models have undergone significant development in recent years. The technical details of these developments are described in Roeckner et al. (2003) (for the atmosphere component) and, for the ocean model, in Marsland et al. (2003). Here we describe results from a version of the model that serves as a prototype for the IPCC AR4 simulations. The atmosphere model uses the cycle 5.2 of the ECHAM model family (ECHAM5.2) and is run at T63 resolution (1.875° × 1.875°) with 31 vertical (hybrid) levels. The ocean has 1.5° average horizontal grid spacing with 40 unevenly spaced vertical levels. A 300 year present-day climate control simulation run without flux adjustment is presented concentrating on the analysis of key climate variables such as sea surface temperature (SST), sea ice concentration and extents, oceanic heat and freshwater transports and water mass transformations.

The accurate simulation of the equatorial SST climatology is crucial for a proper representation of the El Niño Southern Oscillation (ENSO). A previous version of the model (Keenlyside et al., 2004) showed a pronounced cold bias in the equatorial Pacific, where the SST error in the western Pacific exceeded 4 K. A number of attempts to improve the model by modifications to the physical parameterizations of friction and diffusion turned out to be largely unsuccessful. As has been found in the El Niño Simulation Intercomparson Project (ENSIP), the equatorial cold/warm bias is a problem common to many coupled models (Latif et al., 2001) and is related to the amplification of model errors by coupled feedbacks leading to an over/under estimation of the divergence of equatorial ocean currents and associated upwelling. Although ENSO originates in the tropics, it affects both the mean and the

variability of global climate. Latif et al. (2000) showed that tropical feedbacks even influence the stability of the THC. Reducing the easterly winds at the equator will certainly reduce the wind driven ocean currents, their divergence and the associated upwelling. While many studies have emphasized the sensitivity of stress to surface drag (e.g. Large and Pond, 1981) there are only a few papers that deal with the impact of ocean currents on wind stress. Pacanowski (1987) suggested that wind stress be calculated from the velocity difference between the near surface wind speed and the ocean current. He found significant changes in equatorial SST and in the seasonal cycle of the upwelling in a model experiment forced by climatological wind stress when the ocean currents were taken into account in the stress calculation. However, this approach did not find a widespread application in coupled ocean atmosphere models. We have implemented such a parameterization in our coupled model, following Luo et al. (2005).

The paper is structured as follows. The ocean model, the formulation of the parameterization for wind stress, and the experiments performed are described in section 2. In section 3, the model's climatology is compared with observations and in section 4, the simulation of tropical interannual variability is presented. The impacts of the new parameterization on the mean state and on interannual variability are described in the respective sections. A summary is presented in section 5.

2. The ocean and sea-ice model

Technical details of the ocean model MPI-OM and the parameterizations that have been implemented during the transition from the Hamburg Ocean Primitive Equation (HOPE) model (Wolff et al., 1997) to the MPI-OM model can be found in Marsland et al. (2003). Here we summarize the main features. The primitive equations for a hydrostatic Boussinesq fluid are formulated with a free surface. The vertical discretization is on z-levels and the

bottom topography is resolved by way of partial grid cells (Wolff et al., 1997). Using the formulation of Arakawa and Lamb (1977) the spatial arrangement of scalar and vector variables is formulated on a C-grid.

The along-isopycnal diffusion is based on the work of Redi (1982) and is implemented following Griffies (1998). The effect of horizontal tracer mixing by advection with the unresolved eddies is parameterized following Gent et al. (1995). For the vertical eddy viscosity and diffusion the Richardson-number dependent scheme of Pacanowski and Philander (1981, PP hereafter) is applied. Since the PP scheme in its classical form underestimates the turbulent mixing close to the surface, an additional wind mixing parameterization is included. The wind stirring near the surface is proportional to the cube of the 10 m wind speed and decays exponentially with depth.

In the presence of static instability, convective overturning is parameterized by greatly enhanced vertical diffusion. A slope convection scheme has been included that allows for a better representation of the flow of statically unstable dense water over sills, such as in Denmark Strait or in the Strait of Gibraltar (see Marsland et al. (2003) for details) and off shelves, such as on the Arctic and Antarctic shelves.

The dynamic and thermodynamic sea ice model is similar to the earlier HOPE model (Wolff et al., 1997). The dynamics of sea ice are formulated using viscous-plastic rheology following Hibler (1979). The thermodynamics relate changes in sea ice thickness to a balance of radiant, turbulent, and oceanic heat fluxes. The effect of snow accumulation on sea ice is included, along with snow-ice transformation when the snow/ice interface sinks below the sea level due to snow loading. The effect of ice formation and melting is accounted for within the model assuming a sea ice salinity of 5 psu.

An orthogonal curvilinear grid allows for an arbitrary placement of the grid poles. In the current set-up, the model's North Pole is shifted to Greenland and the South Pole is moved

toward the center of the Antarctic continent (Figure 1). This approach not only removes the numerical singularity associated with the convergence of meridians at the geographical North Pole but also produces higher resolution in the deep water formation regions near Greenland (Greenland Sea, Labrador Sea) and in the Weddell Sea. In fact, the grid spacing is at minimum with about 15 km around Greenland and at maximum with 184 km in the Pacific. The topography was interpolated from the ETOPO5 (National Geophysical Data Center, 1988) 1/12° dataset and specific topographic features, such as the important conduits of overflows and throughflows, were adjusted to observed sill depths.

Atmosphere and ocean are coupled by means of the OASIS coupler (Valcke et al., 2003). The ocean passes the sea surface temperature (SST), sea ice concentration, sea ice thickness, snow depth, and the ocean surface velocities to the atmosphere. River runoff and glacier calving are treated interactively in the atmosphere model and the respective fresh water fluxes are passed to the ocean as part of the atmospheric freshwater flux field. The land hydrology model includes a river routing scheme (Hagemann and Dümenil-Gates, 1998, 2003), but the mass balance of glacier ice sheets is not accounted for in this model. Snowfall onto glaciers is, therefore, directly transferred to adjacent ocean points. None of the experiments described below require the use of flux adjustment.

2.2 The effect of ocean currents on wind stress

The surface wind speed is typically one or two orders of magnitude larger than the surface currents over much of the ocean. In equatorial regions, however, oceanic surface speeds can exceed 1 ms^{-1} (e.g. Weisberg, 1984) while typical wind speeds are about 5-6 ms^{-1} (Halpern, 1988). For this reason, Pacanowski (1987) suggested that wind stress calculations should take into account the surface wind relative to the underlying ocean flow:

$$\boldsymbol{\tau = \rho C_D \, |W-V| \, (W-V)}$$

where ρ and C_D are the density of air and the drag coefficient, **W** is the lowest level wind vector and **V** is the ocean velocity vector, respectively. Kelly et al. (2001) compared satellite derived scatterometer data with those from the Tropical Atmosphere Ocean (TAO) array and found that the differences between both products can be as large as 50%. The role of the ocean currents in causing this discrepancy (at least in the tropics) is supported by the strong relationship between the TOA-measured surface motion and the differences in the respective wind measurements. Pacanowski (1987) implemented the ocean current effect on the wind stress calculation into an ocean model that was forced by climatological wind velocities. In his study, an application to the tropical Atlantic Ocean showed the following effects: the westward surface currents that are in the same direction as the wind stress were reduced by about 30%, the North Equatorial Counter Current was also reduced and the equatorial upwelling decreased significantly. As a result there was a warming near the equator of about 1 K and cross equatorial current profile simulation was in closer agreement with measurements.

Recently, Luo et al. (2005) have improved the equatorial cold bias in the Scale INTeraction Experiment (SINTEX-F) coupled model by allowing for momentum transfer of the ocean currents to the atmosphere. We have adopted Luo et al's "fully coupled" Wind Stress Correction (WSC) because this method reduced the cold bias much more than the "semi-coupled" version where the ocean currents enter only the bulk formulae for the wind stress calculation. In fact, in the "fully coupled" approach, the ocean velocities enter the wind stress calculations in two ways. Firstly, the calculation of the vertical shear owing to friction is modified by using the ocean velocities as lower boundary conditions, rather than assuming a non-moving surface. Secondly, the relative motion between the lowest atmospheric layer and the ocean surface is used in the calculation of the drag coefficient (and other turbulent mixing coefficients) assuming a law-of-the-wall formulation (Roeckner et al., 2003). Apart

from the momentum fluxes, the 10 m wind speed entering the calculation of the turbulent mixing in the upper layers of the ocean is modified accordingly. In the presence of sea ice, a similar modification is used for the air-ice stresses.

The SINTEX-F model described by Luo et al. (2005) has a relatively high resolution (T 106 in the atmosphere) and, since it doesn't include a sea ice model, is mainly used for low to mid-latitude interaction studies. Here, we apply the WSC to a state-of-the art climate model that is used for long-time integrations and climate change projections.

Two coupled experiments are performed in the present study. The standard run, on which the analysis of the mean state and the tropical variability is based, includes the parameterization for the effect of ocean surface currents on the wind speeds. This experiment is called WSC, whereas the respective run without this parameterization is named NWSC (No Wind Stress Correction). Both experiments are run until the model year 300 but WSC is started from the output of year 77 of the NWSC experiment. NWSC, in turn, is started using the output of a climatologically forced ocean-only experiment. We analyze the results for the common period of model years 250-300. For comparison, SSTs and sea ice extents from the Hadley Centre Sea Ice and Sea Surface Temperature data set (HADISST, Rayner et al., 2003) are used.

The time series of globally averaged SST (Figure 2 a) of experiment WSC shows an initial drop of 0.5 K, recovery to roughly the initial value, consistent with the present-day HADISST climatology, and stabilization after about 200 years. Between model years 250 and 300 the long-term temperature change is less than 0.1 K. The initial temperature decrease is caused by changes to the upper ocean water mass properties following the introduction of the wind stress correction parameterization and subsequent changes in upwelling and vertical mixing (see below). The simulated SST in the Niño3-region (5ºS-5ºN, 150ºW-90ºW) is only slightly cooler than the observations from the last 20 years of the 20th century. Neither the

mean SST nor the envelope of the extremes shows significant trends over the last 100 years of the experiment. Although the simulation of tropical variability has been much improved compared to earlier versions of the MPI-M model and other AOGCMs (see VanOldenborgh et al., 2005) the simulation overestimates the magnitude of the extremes. In particular, the cold (La Niña) events are approximately as strong and frequent as the warm El Niño events (see below). Northern Hemisphere sea ice extent (Figure 2 c) has a simulated annual mean of 9.7×10^{12} m^2, slightly smaller than the annual mean from the HADISST data (Figure 2 d). Notice, however, the drift in the observational data during the last two decades of the 20^{th} century that is most likely caused by multidecadal variability of the North Atlantic/Arctic climate system (Polyakov and Johnson, 2000). While the monthly mean data indicate that the model simulates the summer extent well, the winter ice area is always smaller than the lowest winter estimate from the HADISST data. In the Southern Hemisphere, the model reproduces the observed annual mean of about 10×10^{12} m^2 and the summer ice extent well. Here, however, the winter maxima are about 10% higher than the climatological values. As will be shown below, there is too much ice spread northward into the Atlantic sector of the Southern Ocean. Generally, there is no significant trend in the ice area time series, indicating a well-balanced system.

Globally averaged subsurface temperature deviations from the Polar Science Center Hydrographic Climatology (PHC, Steele at al., 2001) climatology are relatively small at the beginning of the coupled experiment whereas initial salinity errors are larger, carried over from the climatologically forced ocean-only experiment (not shown). The distribution is consistent with the error patterns found in the uncoupled simulation of Marsland et al. (2003) and can be attributed to the inability of the model to maintain intermediate water mass properties in the Atlantic and the Pacific. There is a considerable drift in the temperature at intermediate and deep water levels that occurs during the coupled experiment. As a result, the

model produces too warm and too salty deep water masses. This drift has, however, no pronounced effect on the Thermohaline Circulation (THC).

3. The mean state

Sea surface temperature and sea ice are the most important ocean variables for the determination of the atmosphere to ocean fluxes and the realism of the coupling and atmosphere-ocean fresh water fluxes are sensitive indicators of coupled model performance. The difference between modeled surface temperature averaged over the last 50 years of the simulation WSC, and the AMIP surface temperature is shown in Figure 3 a. The deviation from the observed values is less than 1K over much of the ocean. There are certain areas, however, where the discrepancy is considerably larger. The strongest bias is seen over the North Atlantic. The pathway of the North Atlantic Current (NAC) across the Atlantic is more zonally oriented than that observed, leading to a pronounced cold bias in the transition region between subtropical and subpolar gyres. On the other hand, the NAC transports too much heat (and salt, not shown) into the Nordic Seas and onto the Barents Shelf leading to too warm surface conditions there. Also, the Irminger and Labrador Seas in the northwestern Atlantic are too warm. Apparently, the NAC loses too little heat to the atmosphere over the subpolar North Atlantic. Errors of similar magnitude, but opposite sign, occur in the Kuroshio region. A shift in the position of the Pacific boundary current system that is associated with large horizontal SST gradients leads to pronounced errors.

Positive SST biases occur at the western coasts of the Americas and Africa. This is a consequence of the lack of sufficient stratocumulus clouds in the atmosphere model, a feature that is widespread among state of the art coupled models (e.g. Barthelet et al., 1998; Gordon et al., 2000; Washington et al., 2000; Roberts et al., 2004). Finally, there are discrepancies in the Southern Ocean. In the Indian Ocean sector and the Australian sector, the SST is too high near Antarctica and too low on the northern flank of the Antarctic Circumpolar Current

(ACC). The SST errors here are most likely caused by deficiencies in the simulation of the mixing of surface waters and the underlying Circumpolar Deep Waters (CDW) and errors in the position of the ACC. The SST in the central Pacific is off by slightly more than 1 K but matches the HADISST data well in the western Pacific. Compared to earlier model versions and other coupled models (Latif et al., 2001; Kiehl and Gent, 2004) the cold bias in the equatorial Pacific is much improved. As discussed below, the new parameterization for wind stress is a major contributor to this improvement, which is in agreement with another modeling study (Luo et al., 2005).

Precipitation is one of the most important climate variables and the proper simulation of patterns and variability is still a challenge for coupled global climate models (Mechoso et al., 1995; Dai, 2006). One outstanding feature is the so-called double Inter Tropical Convergence Zone (ITCZ). In the Pacific, most models (without flux adjustment) simulate two perennial zonal bands of maximum precipitation straddling the equator, whereas in nature there is only a seasonal double ITCZ in the eastern Pacific. The simulation presented here is no exception as can be seen from the differences between the model precipitation and the Xie and Arkin (1997) observations (Figure 3 b). The northern ITCZ is shifted too much to the North and is too broad. There exist a dry bias directly over the equator, where SSTs are still too cold. South of the equator, there is a zonally-oriented rainfall maximum that extends almost all the way to the South American coast. The southern ITCZ is accompanied by a overly dry region to the south west of it. This pattern reflects the inability of the model to correctly simulate the precipitation pattern of the South Pacific Convergence Zone (SPCZ). Recently, Li et al. (2004) have analyzed several processes involved in the modeled double ITCZs. Their sensitivity studies show that two problems, still present in modern GCMs, lead to the erroneous structures: the overestimated zonal wind stresses and erroneous equatorial zonal SST gradient on the one hand, and the warm bias of SSTs off the South American coast on

the other hand. As will be shown below, the first process is affected positively by the application of the WSC. The second mechanism, which involves the underestimation of low-level stratus off the Peruvian coast, is, however, a persistent problem also in our model (see also Dai, 2006).

A realistic simulation of sea ice is crucial for a climate model because of the insulating effect of the ice cover and the ice-albedo feedback. Simulated sea ice concentrations are compared with monthly sea ice concentrations included in the HADISST data set. The data for the Arctic are provided on a 1° grid and cover the period 1870-2003. Here we use only the data from the years 1978 to 2003 because these are based on satellite data (Rayner et al., 2003). The modeled ice extent and its seasonal variation compares favorable with observations. In the Northern Hemisphere (Figure 4 a-d), the impact of the oceanic circulation on the ice coverage can be clearly seen. The warm Norwegian Atlantic current splits up into one branch that enters the Barents Shelf and the West Spitsbergen Current. As a result, the Barents Shelf and the western coast of Svalbard remain largely ice free in winter (Figure 4 b). Although the model underestimates the widths of the ice covered region to the east of Greenland, the southward extent of the ice edge just to Cape Farewell is well reproduced. The eastern part of the Labrador Sea remains ice-free allowing for intensive air-sea exchange there. Both the simulation and the observations suggest that the winter ice concentration exceeds 90% for most of the ice-covered region. The model reproduces well the retreat of the sea ice boundary in summer: In September, the Barents and Kara Seas are largely ice-free. The model underestimates, however, the melting on the Siberian and Canadian Shelves where the observations indicate ice concentrations less than 30% near the coasts whilst simulated concentrations are lower than observed in the central Arctic. This reflects deficiencies in the simulation of the atmospheric wind field and the associated ice motion. Simulated sea ice circulation in late winter and late summer (Figure 4 b, d) can, to a

certain extent, be compared to the long-term average ice motion figures that were derived from Special Sensor Microwave/Imager (SSM/I) data by Emery et al. (1997, their Figure 1). The simulated sea ice drift in the Arctic includes the well-known features, such as the Transpolar Drift Stream (TDS) and the anticyclonic gyre in the Canadian Basin. A convenient feature of the placement of the grid poles over land is that there is no need for a special numerical treatment of the pole. Ocean models, which use a regular geographical grid often place an island directly onto the North Pole, artificially diverting the flow around the pole. Compared to the satellite derived SSM/I data (Emery et al., 1997) and reconstructed circulation schemes (e.g. Colony and Thorndike, 1984) our simulated anticyclonic Beaufort Gyre, which is, in reality, confined to the Beaufort Sea, extents too far into the central Arctic. The TDS is therefore shifted too far to the European Basin. This shift is even more pronounced in summer (Figure 4d), where the center of anticyclonic motion spreads out even more towards the North Pole. This simulated seasonal change does not agree with the buoy-drift figures presented by Proshutinsky et al. (2002), who report a weakening of the Beaufort Gyre in summer but not a spatial shift. The ice transports largely reflect the overlying atmospheric circulation. In the simulation, the polar high is slightly too weak and located over the central Arctic in winter.

In the SSM/I data, the TDS is supplied primarily from Siberian coastal waters rather than from the Beaufort Gyre. However, the model captures well the ice flow exiting from the Kara Sea that turns southward near Franz Josef Land and flows into the Barents Sea in winter. The model has two openings in the Canadian Archipelago, the passage from McClure Strait to Lancaster Sound and the Nares Strait between Ellesmere Island and Western Greenland. The major part of the Arctic ice exports towards the North Atlantic takes, however, the path through Fram Strait. The average Fram Strait ice export of 2618 km^3yr^{-1} lies well in the range

of observational estimates. Aagaard and Carmack (1989) calculated 2790 km^3yr^{-1}, Vinje (2001) reported 2900 km^3yr^{-1}, and Kwok et al. (2004) gave an estimate of 2218 km^3yr^{-1}.

The Southern Hemisphere ice concentrations (Figure 4 e-h) are generally well simulated compared to the climatology, both in the seasonal variation and in the mean distribution. The model tends to underestimate the ice concentration in the Weddell Sea and the Ross Sea in winter. In particular, the austral winter concentration in the Weddell Sea gyre is reduced to values less than 50%, indicating the occasional presence of open water (polynya). A further inspection of the HADISST sea ice data for the early 1970s (that did not enter Figure 4g) confirms that such polynya situations indeed occur in reality. In the model, low ice concentrations occur in the center of the clockwise rotating Weddell Sea Gyre and indicate that relatively warm water is brought to the surface by convection (c.f. Figure 5). In the Atlantic sector, the sea ice is spread out too far to the north with the clockwise rotating Weddell Sea gyre that appears to be too strong. In austral summer, the simulation successfully reproduces the year-long presence of sea ice around the continent. The model slightly underestimates the ice extent off the Ross Sea and to the west of the Antarctic Peninsula. Also, in the Southern Hemisphere, the simulated ice motion captures the general patterns of Antarctic ice motion (e.g., Emery et al., 1997). The center of the Weddell Sea Gyre and the Ross Sea Gyre are placed approximately correctly when compared to the SSM/I data of Emery et al. (1997, their figure 2). There is a nearly continuous westward flow along the coast (the East Wind Drift) that, in some places (e.g. in the Ross Sea), bifurcates into clockwise rotating gyres.

Deep water formation in the Northern Hemisphere takes place both to the north and to the south of the Greenland-Scotland Ridge. Figure 5 shows the maximum depth of convection, diagnosed as the deepest model layer where the (diffusive) convection parameterization was active. In the Nordic Seas, convection exceeding 1000 m is widespread in the Greenland and

Iceland Sea with maxima exceeding 1500m in the Iceland Sea. The model fails to reproduce the convection in the central Greenland Sea gyre where too warm surface temperatures prevail (Figure 3). The convective region to the south of Greenland extends from the Labrador Sea (LS) to the southeast, whereas it is much more confined to the LS in observations (e.g. Pickart et al., 2002). There is considerable temporal variation in the regional extent that is associated with changes in the subpolar gyre position variations of the atmospheric pressure field that are similar to the North Atlantic Oscillation (NAO). In the Southern Hemisphere, convection to abyssal depth occurs in the Weddell Sea but also at some grid points in the Ross Sea. A surface manifestation of the convection is the relatively low ice concentration in the central Weddell Gyre in the 50-year average shown in Figure 4. Although open ocean convection has been observed in the Weddell Sea (Gordon, 1978) the observations are limited in time and space. In reality, most of the Antarctic Bottom Water (AABW) is formed on the shelves during polynya conditions (Orsi et al., 1999). As has been shown by Marsland et al. (2004), high resolution and an adequate representation of topographic details are required to realistically simulate high rates of sea ice growth and brine rejection. The evolution of the simulated water mass properties (too warm) and spreading rates of AABW indicates that the bottom water formation rate is too small in our model (not shown).

The time-averaged barotropic stream function reproduces the known general circulation features and gyre systems and is not reproduced here. Compared to observations, however, the path of the Gulf Stream extension (the North Atlantic Current (NAC)) is too zonal. This is largely related to insufficient resolution that does not allow for a Gulf Stream separation at Cape Hateras and a proper representation of the pathway of the Deep Western Boundary Current (DWBC) (C. Boening, pers. communication). As a result, the simulated circulation does not capture the North West Corner where the NAC in reality turns north and the

subpolar gyre is spread out too far to the east. The mass flux through Drake Passage of 165 Sv ($1Sv = 10^6 m^3 s^{-1}$), exceeds the estimates of 134±14 Sv from Nowlin and Klinck (1986). The throughflow between Australia and Antarctica is about 170 Sv compared to 147±10 Sv estimated from repeated sections by Rintoul and Sokolov (2001). The strength of the ACC depends on the resolution of topographic details, such as the South Sandwich Islands, and on the choice of isopycnal diffusivity (Gent et al., 1998; Gent et al., 2001). Other large-scale oceanic volume transports are as follows: Florida Strait transport is about 24 Sv, compared to an estimate of about 32 Sv by Larsen et al. (1992), the Indonesian throughflow is 13 Sv where Wijffels et al. (1996) give an estimate of 7±12 Sv. The relatively dense waters flow (σ_θ 27.8) through the Denmark Strait and the Faeroe Bank Channels form the core of the lower North Atlantic Deep Waters (NADW). In the model, overflow transport rates at the sills are close to 2.5 Sv and 2 Sv, respectively, in agreement with observations (Ross, 1984; Saunders, 1990). As was demonstrated by Marsland et al. (2003) the newly implemented bottom boundary layer scheme improves the water mass properties as the overflows descend the steep slopes of the sill and mix with ambient waters.

The large-scale ocean transports can further be visualized by the meridional stream function calculated from the mean velocities. The zonally integrated Atlantic streamfunction in latitude-depth space shows the tropical-subtropical overturning cells with their usual asymmetry about the Equator (Figure 6). The conveyor-belt circulation is represented by the clockwise-rotating cell associated with the formation of NADW in the North Atlantic and the counterclockwise rotating Antarctic Bottom Water (AABW) cell. In the Atlantic, the NADW cell reaches a maximum of 18.5 Sv at about 40°N at a depth of 1000 m. This compares well with the observational estimates of 18±4 Sv (Macdonald, 1998) and 18 Sv (Talley et al., 2003). Across the southern boundary of the Atlantic more than 15 Sv are exported. The AABW cell in the Atlantic has a maximum of about 3.3 Sv and about 3 Sv enter the South

Atlantic at 30°N. Compared to estimates from inverse models the AABW rates are rather low. Sloyan and Rintoul (2001) and Ganachaud and Wunsch (2000) suggested an AABW inflow of about 6 Sv from geostrophic velocity estimates. Moreover, the AABW cell weakens considerably over the course of the experiment from more than 5 Sv to 3.3 Sv. Apparently, the formation of AABW with correct water mass properties is insufficient in this model owing to insufficient bottom water formation on the Antarctic shelves. On the other hand, the strength and structure of the NADW cell is quite stable.

The simulated global heat transports compare favorably with the estimates from direct observations and inverse calculations (Figures 7 a, c). The maximum poleward heat transports are 1.8 PW near 26°N in the Northern Hemisphere and -1.7 PW near 10° S in the Southern Hemisphere. In the Atlantic, the simulated transports are within the range of uncertainty of the Trenberth and Solomon (1994) estimates but fail to reproduce the numbers that come from inverse calculations (e.g., Ganachaud and Wunsch's (2003) estimate of 1.27±0.15 PW at 24°N). The global heat flux imbalance of nearly 0.4 PW (~ 1 W per square meter of ocean surface) reflects the heat uptake by the deep ocean that has not yet equilibrated. This number is of the same order as the estimated upper ocean (0-750 m) warming estimated from the 1993-2003 observations by Willis et al., 2004.

Observational estimates of fresh water fluxes usually have large uncertainties, and indirect calculations from observation-based climatologies (e.g. Josey et al., 1996; Da Silva et al., 1994) show considerable differences (Wijffels, 2001). The simulated global meridional fresh water transport (Figure 7 b), as implied from the long-term average of the atmosphere to ocean fresh water flux, reproduces the general features of the estimates from inverse calculations, such as the latitudes of sign changes. However, the simulated maximum of 1.25 Sv around 40ºS exceeds the direct and indirect estimates discussed in Wijffels (2001). In the

Atlantic (Figure 7 d), the most robust discrepancy between the observational estimates and the simulation is the much too negative fresh water flux poleward of 30ºN.

We now quantify the impact of the new wind stress parameterization on the mean state (defined here as the 250-300 year average) by comparing the experiment WSC with an otherwise identical simulation without the wind shear correction (NWSC). The impact of the parameterization can be thought of as arising from two effects. The first, and most straightforward to understand, is simply due to the change in the magnitude (and curl) of the wind stress seen by the ocean. The second, which is non-trivial to diagnose, is due to changes in the feedbacks between the ocean and the atmosphere, e.g. due to changes in atmospheric and oceanic sensitivity that result either from the direct effect of the atmosphere being influenced by the ocean currents, or from changes in the mean state itself. As expected, the parameterization affects the wind stress curl (Figure 8 a) mostly where ocean speeds are high. In the Southern Ocean, winds and the upper layer of the ocean move in the same direction so that there is both a reduction of (the usually positive) wind stress curl on the northern flank of the ACC and a reduction of negative stress curl anomalies to the south of the ACC axis. There is also a clear effect in the regions of the boundary currents on the eastern coasts of the continents, such as the North Brazil Current and the Gulf Stream-North Atlantic Current. Whereas there are only minor changes in the wind stress curl in the equatorial Atlantic, the changes in the Pacific equatorial current /wind system leave a clear imprint on the wind stress curl distribution. The changes are mainly due to a reduction of the westward component of the wind stress. The reduction of the westerly wind stress anomalies in the ACC region is associated with a reduction of easterly wind stress anomalies in the Tropics by means of the global angular momentum balance. The gain of angular momentum in the Tropics must be balanced by loss in the extratropics (Luo et al., 2005). The sensitivity experiments in Luo et

al. (2005) show that the influence of the atmospheric general circulation adjustment contributes significantly to the reduction of the easterly trade winds.

Figure 8 b shows the changes in the sea surface temperatures. Large positive changes in the western and central equatorial Pacific are apparent, where the cold bias is reduced by more than 1 K. As a result, SST deviations from the HADISST climatology (Figure 3 a) are relatively small in the warm pool. Comparing Figure 8 b and Figure 3 a further indicates that the SST errors in the Barents Sea, near Bering Strait and in the Weddell and Ross Seas would be larger without the new parameterization. There is only slight improvement in the warm-bias zones off the western coasts of South America and off South Africa. Moreover, near the Peruvian coast, the modified wind stresses do not favor enhanced upwelling so that the cooler SSTs must be due to changes in frontal positions and/or changed atmospheric conditions (in contrast to Luo et al.'s (2005) findings). Although Figure 8 a showed considerable changes in the wind stress curl over the boundary region of the subtropical and subpolar gyres in the North Atlantic, there is no improvement in the too cold North Atlantic where the SST errors are more likely due to shortcomings in the ocean resolution.

A comparison of the precipitation changes between WSC and NWSC reveals most pronounced differences in the equatorial regions of the Pacific and Indian Ocean. In the western Pacific, the dry bias is reduced by up to 2.5 mm/day (roughly 30%), but not eliminated (c.f. Fig. 3 b). This supports the finding of Li et al. (2004) who stated that the equatorial component of the double ITCZ phenomenon is related to overestimation of the easterly winds in the central equatorial Pacific. There is also a slight reduction in the wet bias to the south of the Equator in the central Pacific. Here, where we only see a slight improvement of the overly warm SSTs (c.f., Figure 3 a), the model still produces a southern ITCZ and fails to reproduce the typical northwest-southeast orientation of the rainfall maximum associated with the SPCZ. Li et al. (2004) have pointed out that the southern ITCZ

in the models is mainly related to the warm bias in the surface waters which originate from the lack in stratocumulus clouds off the coast of South America.

In the equatorial Pacific, the new wind stress parameterization leads to a pronounced reduction in zonal wind stress (Figure 9). At the equator, the wind stress reduction is largest in the western and central Pacific. The resulting convergence (Figure 9b) leads to more pronounced convective precipitation over the warmer western Pacific (Figure 8 c). There is an intensification of the winds blowing toward the equator to the east of Australia caused by the now warmer SST in the western Pacific. Weaker equatorial surface stresses are to be expected, since, at the equator, the ocean currents and surface Trade Winds are both westward. The Trade Winds drive the surface westward current, the South Equatorial Current (SEC), and also induce poleward Ekman transports and equatorial upwelling. Reduced wind stresses thus produce a weaker equatorial circulation and divergence. In the western Pacific Ocean, ocean surface speeds are reduced by more than 0.4 ms^{-1} (not shown). Equatorial upwelling is reduced across the basin, with the largest changes in the western Pacific and near Indonesia (Figure 9 c). In the central Pacific, the mean equatorial upwelling at 50m is around $2x10^{-5}$ ms^{-1} (~630 myr^{-1}), which corresponds to a 30 percent reduction as compared to the NWSC run and is well within the range of observational estimates (e.g., Weisberg and Qiao, 2000) and consistent with other models (e.g., Large et al., 2001).

These changes modify the mean equatorial mixed layer heat budget. The temperature tendency from various contributions is stored in the model and time averages, integrated over the upper 50m (used as an estimate of the mean mixed layer depth (Huang and Liu, 2002; Vialard et al., 2001)), are displayed in Figure 10. The total temperature tendency is small in the long term mean. In the eastern equatorial Pacific, the mixed layer temperature is maintained by warming by surface heat fluxes and meridional advection and cooling by vertical advection (upwelling) through the mixed layer base. In the western Pacific, the

balance is made up by surface warming and cooling by zonal advection and upwelling. While the structure and magnitude of the surface flux and vertical advection terms compare relatively well with the hindcast simulation of Vialard et al. (2001) the horizontal advection contributions do not appear to be realistic. This is related to the much lower resolution of our model and the poor representation of the surface currents. Comparing the WSC and the NSWSC simulations we find the most pronounced changes in the contributions from the heat flux divergences. The changes in the horizontal advection terms act to warm the equatorial Pacific. Directly at the equator, the zonal advection contribution is reduced by roughly 50%. The vertical advection is also reduced but the warming effect appears only in the western Pacific owing to changes in the thermocline depth. There is less mixing necessary to balance the advective heat contributions in the regions off the equator (Luo et al., 2005). In the western Pacific, the now warmer SSTs have a damping effect on the surface heat fluxes (Figures 10 a, b).

As equatorial upwelling is reduced, the warmer SST in this region is consistent with the atmospheric circulation changes. Thus, the sign of the changes in equatorial Pacific atmosphere and ocean are easily understood. The magnitude of the changes is, however, strongly modulated by the Bjerknes feedback, which relates changes in zonal wind stress, upwelling, and SST. However, the structure of the mean surface currents is relatively poor, with the simulated SEC having a maximum on the equator, in contrast to the observed minimum (not shown). The simulated equatorial undercurrent (EUC) is insensitive to the new parameterization. Due to the model's coarse meridional resolution of approximately 1.5º, the model's EUC is 50% too weak (having a maximum eastward velocity of about $0.4 ms^{-1}$) and meridionally too diffuse. In contrast, the simulated equatorial thermal structure is in good agreement with observations. The mean depth of the 20-degree isotherm along the equator matches the Levitus et al. (1998) climatology well, and the thermocline is only slightly too

diffuse. The slope and sharpness of the thermocline are improved over the NWSC simulation, with the largest differences in the western/central Pacific where the thermocline is some 30 meters shallower (not shown) in the WSC case (i.e., the east west tilt is reduced consistent with the weaker zonal winds).

4. Simulation of tropical variability

In this section, the simulated interannual variability of the tropical Pacific is described. The statistics for the Niño 3 monthly-mean anomalies (Table 1) indicate that, although the variability is drastically reduced in the WSC compared to the NWSC run, the standard deviation of the simulated SSTs is still roughly 0.5 K higher than the respective ones from HADISST. Moreover, the higher moments, which indicate the "non-normality" (Burgers and Stephenson, 1999) of ENSO, deviate significantly from the observed data. There is no predominance of El Niño events compared to La Niña events and the simulated time series are more or less normally distributed. In the higher moments, we don't see any improvement from the NWSC to the WSC experiment. The reason why the model underestimates the degree of non-linearity in ENSO is not clear and more research is necessary to understand the underlying physics. Compared to the NWSC run, the spectral peak of the WSC Niño 3 time series is shifted from 3 to 4 years, more close to the 4-6 years band that characterizes the dominant ENSO period in the observations (Figure 11).

The model's annual cycle of equatorial SST is characterized by a weak semi-annual cycle in the west, and a strong westward propagating annual cycle in the east (Figure 12 a, b). In the west, the phase and strength match observations well. In the east, the strength is well simulated but the positive phase lags observations by 1-2 months, and the negative phase slightly leads observations. This is an improvement on an earlier version of the model (Keenlyside et al., 2004) and resembles the better-performing models of the ENSIP (Latif et al., 2001). However, this improvement is not due to the shear correction, and is more likely

related to changes in the mean state, which were much larger between the old and new versions of the model (most likely due to improvement in resolution in the atmosphere model going from a T42 - 19 level to a T63 - 31 level set-up) than between the WSC and NWSC experiments. The link between the mean state and the annual cycle has been demonstrated in other modeling studies (e.g., Li and Philander 1996). The simulated variability is, however, less related to the annual cycle and does not show the pronounced phase-locking that is obvious in the observations. In the WSC experiment, the model simulated standard deviations as a function of calendar month (Figure 12 c) is more flat, but shows minimum standard deviations in April, as in the observations. In the NWSC set-up, the minimum is shifted into summer and there is an even more pronounced second minimum in autumn.

The spatial pattern of interannual SST variability is portrayed by the correlation between Niño3 SST anomalies and global SST anomalies (Figure 13). In the Pacific, there is good agreement with correlations obtained from observations (HADISST) with realistic meridional structure and strength, the westward extension of variability in the model is, however, too strong. Teleconnected variability is broadly consistent with observations, although discrepancies occur in the equatorial Atlantic and Indian oceans. Experiments with other AOGCMs indicate that atmospheric resolution is an important factor obtaining a realistic spatial pattern of tropical Pacific interannual SST variability (Gualdi et al., 2003). A recent intercomparison study by VanOldenborgh et al. (2005) of 20 IPCC AR4 models has confirmed that the ECHAM5/MPI-OM coupled model produces relatively realistic ENSO variability. Given the ocean's coarse meridional resolution in the tropics, these results support the idea that the atmosphere plays a dominant role in determining important characteristics of interannual SST variability (Guilyardi et al., 2004).

Relative to the NWSC run, there have been several improvements in the simulation of interannual variability. Equatorial SST variability is dominated by unrealistically strong

westward propagation in NWSC (Figure 14, middle panel), unlike the WSC simulation (right panel). The strength of the variability is weakened by about 30% in the eastern and central Pacific, and the westward extension of the variability into the warm pool is much reduced (Figure 14). The mechanism of this damping feedback is easily understood: wind anomalies introduce surface current anomalies in the same direction that, in turn, reduce the wind stress anomalies.

Pacific equatorial SST anomalies in the WSC experiment are simulated with an almost standing east-west pattern. Individual events, however, exhibit significant differences, and interdecadal changes in ENSO characteristics are also simulated. In particular, there are strong positive events, which propagate eastwards (e.g., model year 273), weak positive events that are confined to the central western Pacific (e.g., around year 270), and periods characterized by weak westward propagation (e.g., model year 255). Negative events also tend to be westward propagating. All these features are reminiscent of observations.
While significant progress has been made in understanding the factors controlling ENSO period and its damped/undamped nature, the factors which control its amplitude are not well understood. However, it is tacitly understood that changes in the relevant positive/negative feedbacks will impact ENSO amplitude (as well as period). These changes may be induced through changes in the mean state. For example, experiments with other AOGCMs indicate that ocean background diffusivity, which affects the thermal structure, can strongly affect ENSO amplitude (Meehl el al. 2001).

The feedbacks relevant to the delayed oscillator framework have been estimated in the two simulations using scatter plots and regression analysis among anomalies of SST, τ_x, thermocline depth, and net surface heat flux. The analysis suggests that one reason for the reduced variability is an approximately10% reduction of atmospheric (central Pacific zonal wind stress) sensitivity to eastern Pacific SST (Figure 15). Despite the 30% reduction in

equatorial upwelling in the central Pacific, the eastern Pacific SST-thermocline feedback is not changed, perhaps due to a slightly sharper thermocline with a weaker east-west gradient. The changes in atmospheric sensitivity are certainly partly due to the direct effect of the atmosphere sensing ocean currents, but may well also be due to changes in the mean state.

Changes in the mean state of the ocean appear to contribute to the reduction in variability in other ways as well, given that the wind shear correction only results in a roughly 10% decrease in atmospheric sensitivity, while there is a 30% reduction in variability. An analysis of the terms controlling interannual SST variability (Table 2) indicates that the relative role of these terms changes with the introduction of the WSC. With WSC, the vertical advection term strengthens and becomes dominant. This is consistent with the diagnosed changes in SST variability. In particular, the SST propagation characteristics are westward in the NWSC (an SST mode characteristic), and more or less stationary in the WSC run (consistent with a thermocline mode). The reduction in variability may also be interpreted as due to a reduction in the strength of the surface horizontal advective terms, and also to the weakening of the atmospheric sensitivity (see above), both of which are consistent with the impact of the WSC, i.e., reduced wind stress and surface current difference.

The improvements in period, propagation characteristics, and westward extension of interannual SST variability in the tropical Pacific are broadly consistent with the theoretical work of Federov and Philander (2001). In particular, there are improvements in the mean state of the model from strong wind/steeper east-west thermocline to a weaker wind / less steep thermocline. A less steep thermocline favors, in the framework of Federov and Philander (2001), a delayed oscillator type mode and a lengthening of the oscillation period.

Luo et al. (2005) have implemented the wind stress correction into the SINTEX-F coupled model consisting of ECHAM4 and the ocean model OPA. Compared to the model used in the present study, the SINTEX model features higher resolution, both in the atmosphere (T106)

and in the equatorial ocean (gradual refinement from 2º to 0.5º). In general, our results confirm the findings of Luo et al. (2005). The equatorial cold bias is significantly reduced in both coupled models. However, there are also differences, for example the increase in upwelling near the Peruvian coast that does not occur in our study. Luo et al. (2005) describe only a slight decrease of ENSO amplitudes whilst we find an order of 30% reduction. These differences are most likely due to differences in the mean state and to the different resolutions. Further improvement of WSC could probably be made by taking into account sub-grid-scale dependencies of ocean currents and wind stress. More analysis, both for the individual models but also a cross-model comparison is, however, needed to better understand the feedback mechanisms.

5. Summary and conclusions

In this article we have discussed the main ocean-related results from a 300 year long integration with the MPI-M coupled climate model ECHAM5/MPI-OM. The simulation of sea surface temperature and sea ice are shown to be stable and realistic. Global-scale heat and fresh water transports are in broad agreement with observations and the improved compatibility of the ocean and atmospheric heat budgets allows for the simulation of a stable climate without flux adjustment. Although there are temperature and salinity drifts in the intermediate and deep ocean the changes in water mass properties are not large enough to seriously influence the large-scale circulation. The North Atlantic overturning circulation and the associated heat and fresh water transports are stable. There is, however, a lack of sufficient Antarctic Bottom Water formation that leads to a significant reduction of the AABW overturning cell. Here, a better simulation of bottom water formation on the Antarctic shelves is needed.

A feature of the current model is that the ocean velocities are taken into account in the calculation of the wind stresses following Luo et al. (2005), rather than assuming an

immobile surface as lower boundary condition. The WSC modification has beneficial effects, mainly in the tropical Pacific. Not only is the cold bias reduced by more than 1 K, there are also improvements in the simulation of tropical variability. The strength of the variability is reduced and the extension of SST variability into the western Pacific is also much reduced. The ENSO period is more realistically simulated, with a dominant period of 4 years. Despite these improvements, the shear correction has no beneficial impact on the simulation of the equatorial annual cycle of SST, the skewness of SST anomalies, or the seasonality of the variability.

The reasons for this and other methods, which could reduce these discrepancies, need to be investigated further. The WSC is a good example of improving model simulations not by tuning individual components, but by improving the coupling physics. Another such example is the inclusion of the effect of phytoplankton on the short wave penetration depth studied by Wetzel et al. (this issue) using a similar model set up, but including the Hamburg Ocean Carbon Cycle model (HAMOCC5). Comparing their model results with a control run with fixed attenuation depth, Wetzel et al. (this issue) find a considerable warming of the entire equatorial Pacific, a reduced ENSO amplitude, and an amplification in the seasonal cycle.

Acknowledgements: The funding for this study was provided by the German Ministry for Education and Research (BMBF) research programs OCEAN CLIVAR and DEKLIM. The model simulations were carried out on the supercomputer facilities of the German Climate Computing Center (DKRZ). The comments and suggestions of two anonymous reviewers were helpful in improving the manuscript.

References

Aagaard, K., and E.C. Carmack, 1989: The role of sea ice and other fresh water in the Arctic circulation. J. Geophys. Res., 94, 14485-14498.

Arakawa, A., and V.R. Lamb, 1977: Computational design of the basic dynamical processes of the UCLA general circulation model. Methods Comput. Phys., 17, 173-265.

Barthelet, P., L. Terray, and S. Valcke: Transient CO2 experiment using the ARPEGE/OPAICE non flux corrected coupled model. Geophys. Res. Lett., 25(13), 2277-2280.

Burgers, G., and D.B. Stephenson, 1999: The "normality" of El Niño. Geophys. Res. Lett., 26(8), 1027-1030.

Colony, R., and A.S. Thorndike, 1984: An estimate of the mean field of Arctic Sea Ice motion. J. Geophys. Res., 89, 10623-10629.

Dai, A., 2006: Precipitation characteristics in eighteen coupled climate models. J. Climate, in press.

Da Silva, A.M., C. Young, and S. Levitus, 1994: Atlas of surface marine data 1994 Volume 1: Algorithms and procedures. NOAA Atlas NESDIS 6,83 pp.

Emery, W.J., C.W. Fowler, J.A. Maslanik, 1997: Satellite-derived maps of Arctic and Antarctic sea ice motion: 1988 to 1994. Geophys. Res. Lett, 24(8), 897-900.

Federov, A. V., and S. G. Philander, 2001: A stability analysis of tropical Ocean-Atmosphere interactions: Bridging measurements and theory for El Nino, J. Climate, 14, 3086-3101.

Ganachaud, A. und C. Wunsch, 2000: Improved estimates of global ocean circulation, heat transport and mixing from hydrographic data. Nature, 408, 453-456.

Ganachaud, A. und C. Wunsch, 2003: Large-scale ocean heat and freshwater transports during the World Ocean Circulation Experiment. J. Climate, 16, 696-705.

Gent, P.R., J. Willebrand, T. McDougall, and J.C. McWilliams, 1995: Parameterizing eddy induced tracer transports in ocean circulation models. J. Phys. Oceanogr., 25, 463-474.

Gent, P.R., F. O. Bryan, G. Donabasoglu, S.C. Doney, W.R. Holland, W.G. Large, and J.C. McWilliams, 1998: The NCAR Climate System Model global ocean component. J. Climate, 11, 1287-1306.

Gent, P.R., W.G. Large, and F. O. Bryan, 2001: What sets the mean transport through Drake Passage? J. Geophys. Res., 106(C2), 2693-2712.

Gordon, A.L., 1978: Deep Antarctic convection west of Maud Rise. J. Phys. Oceanogr., 8, 600-612.

Gordon, C., C. Cooper, C.A. Senior, H. Banks, J.M. Gregory, T.C. Johns, J.F.B. Mitchell, and R.A. Wood, 2000: The simulation of SST, sea ice extents and ocean heat transports in a version of the Hadley Centre coupled model without flux adjustment. Climate Dynamics, 16, 147-168.

Griffies, S.M., 1998: The Gent-McWilliams skew flux. J. Phys. Oceanogr., 28, 831-841.

Gualdi, S., A. Navarra, E. Guilyardi, and P. Delecluse, 2003: Assessment of the tropical Indo-Pacific climate in the SINTEX CGCM. Ann. Geophys., 46, 1-26.

Guilyardi, E., S. Gualdi, J.M. Slingo, A. Navarra, P. Delecluse, J. Cole, G. Madec, M. Roberts, M. Latif, and L. Terray, 2004: Representing El Nino in coupled ocean atmosphere GCMs: the dominat role of the atmosphere model. J. Climate, in press.

Hagemann, S., and L. Dümenil, 1998: A parameterization of the lateral waterflow for the global scale. Clim. Dyn., 14, 17-31.

Hagemann, S., and L. Dümenil-Gates, 2003: An improved sub grid runoff parameterization scheme for climate models. Clim. Dyn., 21, 349-359.

Halpern, D., 1988: Moored surface wind observations at four sites along the Pacific Equator between 140 and 95W. J. Climate, 1, 1251-1260.

Hibler, W.d. III, 1979: A dynamic thermodynamic sea ice model. J. Phys. Oceanogr., 9, 815-846.

Huang, B., and Z. Liu, 2002: An OGCM simulation of seasonal and interannual variabilities in the surface-layer Pacific of the equatorial band. Adv. Atmos. Sci., 19, 219-235.

Intergovernmental Panel on Climate Change (IPCC), 2001: The scientific basis. Contribution of working group I to the third assessment report of the IPCC. J. T. Houghton et al. (Eds.), Cambridge University Press, Cambridge, 2001.

Johns, W.E., T.N. Lee, R.J. Zantopp, and E. Fillenbaum, 1997: Updated transatlantic heat flux at 26.5N. WOCE Newsletter, 27, 15-22.

Josey, S.A., E.C. Kent, D. Oakley, and P.K. Taylor, 1996: A new global air-sea heat and momentum flux climatology. International WOCE Newsletter, 24, 3-5.

Kelly, A.K., S. Dickinson, M.J. McPhaden, and G.C. Johnson, 2001: Ocean currents evident in satellite wind data. Geophys. Res. Lett., 28(8), 2469-2472.

Keenlyside, N., M. Latif, M. Botzet, J. Jungclaus, and U. Schulzweida: 2004: A coupled method for initialising ENSO forecasts using SST data. Tellus, 57A, 340-356.

Kiehl, J.T., and P.R. Gent, 2004: The Community Climate System Model, Version2. J. Climate, 17, 3666-3682.

Kwok, R., G.F. Cunningham, and S.S. Pang, 2004: Fram Strait sea ice outflow, J. Geophys. Res., 109, C01009, doi:10.1029/2003JC001785.

Large, W.G., and S. Pond, 1981: Open ocean momentum flux measurements in moderate to strong winds, J. Phys. Oceanogr., 11, 324-326.

Large, W., G. Danansoglu, J. C. McWilliams, P. Gent, and F. O. Bryan, 2001: Equatorial circulation of a global ocean climate model with anisotropic horizontal viscosity, J. Phys. Oceanogr., 31, 518-536.

Larsen, J.C., 1992: Transport and heat flux of the Florida Current at 27°N derived from cross-stream voltages and profiling data. Philos. Trans. Roy. Soc. London, A338, 169-236.

Latif, M., E. Roeckner, U. Mikolajewicz, and R. Voss, 2000: Tropical stabilization of the thermohaline circulation in a greenhouse warming simulation. J. Clim., 13, 1809-1813.

Latif, M., and 32 coauthors, 2001: ENSIP: the El Nino simulation intercomparison project. Climate Dynamics, 18, 255-276.

Levitus S., T.P. Boyer, M.E. Conkright, T. O'Brien, J. Antonov, C. Stephens, L. Stathopolos, D. Johnson, and R. Gelfeld, World Ocean Database 1998: Volume1: Introduction. NOAA Atlas NESDIS 18, Ocean Climate Laboratory, National Oceanographic Data Center, U.S. Gov. Printing Office, Wash., D.C..

Li, T. M., and S. G. H. Philander, 1996: On the annual cycle of the eastern equatorial Pacific, J. Climate, 9, 2986-2998.

Li, J.L., X.H. Zhang, Y.Q. Yu, and F.S. Dai, 2004: Primary reasoning behind the double ITCZ phenomenon in a coupled ocean-atmosphere general circulation model. Adv. Atmos. Sci., 21, 857-867.

Luo, J.-J., S. Masson, E. Roeckner, G. Madec, and T. Yamagata, 2005: Reducing climatology bias in an ocean-atmosphere CGCM with improved coupling physics. J. Climate, 2344-2360.

Macdonald, A.M., 1998: The global ocean circulation: a hydrographic estimate and regional analysis. Prog. Oceanogr., 41, 281-382.

Macdonald, A.M., and C. Wunsch, 1996: Oceanic estimates of global ocean heat transport. WOCE Newsletter, 24, 5-6.

Marsland, S.J., H. Haak, J.H. Jungclaus, M. Latif, and F. Röske, 2003: The Max- Planck-Institute global ocean/sea ice model with orthogonal curvilinear coordinates. Ocean Modelling, 5, 91-127.

Marsland, S.J., N.L. Bindoff, G.D. Williams, and W.F. Budd, 2004: Modelling water mass formation in the Mertz Glacier Polynya and Adelie Depression, East Antarctic. J. Geophys. Res., 109(C11), DOI: 10.1029/2004JC002441.

Mechoso, C.R., and Coauthors, 1995: The seasonal cycle over the tropical Pacific in coupled ocean atmosphere general circulation models. Mon. Wea. Rev., 123. 2825-2838.

Meehl, G., P. R. Gent, J. M. Arblaster, B. L. Otto-Bliesner, E. C. Brady, and A. Craig, 2001: Factors that affect the amplitude of El Nino in global coupled climate models, Climate Dyn., 17, 515-526.

National Geophysical Data Center, 1988: Digital relief of the surface of the Earth, NOAA, Boulder, Colorado, 1988.

Nowlin, W.D.J., and J.M. Klinck, 1986: The physics of the Antarctic Circumpolar Current. Rev. Geophys., 24, 469-491.

Orsi, A.H., G.C. Johnson, and J.L. Bullister, 1999: Circulation, mixing, and production of Antarctic Bottom Water. Prog. Oceanogr., 43, 55-109.

Pacanowski, R.C., and S.G.H. Philander, 1981: Parameterization of vertical mixing in numerical models of tropical oceans. J. Phys. Oceanogr., 11, 1443-1451.

Pacanowski, R.C.: 1987: Effect of equatorial currents on surface stress. J. Phys. Oceanogr., 17, 833-838.

Pickart, R.S., D.T. Torres, and R. A. Clarke, 2002: Hydrography of the Labrador Sea during active convection. J. Phys. Oceanogr., 32, 428-457.

Polyakov, I.V., and M.A. Johnson, 2000: Arctic decadal and interdecadal variability. Geophys. Res. Lett., 27, 4097-4100.

Proshutinsky, A., R.H. Bourke, and F.A. McLaughlin, 2002: The role of the Beaufort Gyre in Arctic climate variability: Seasonal to decadal climate scales. Geophys. Res. Lett., 29(23), 2100, doi:101029/2002GL015847.

Rayner, N.A., D.E. Parker, E.B. Holton, C.K. Folland, L.V. Alexander, D.P. Rowell, E.C. Kent, and A. Kaplan, 2003: Global analyses of sea surface temperature, sea ice, and night marine air temperature since the late nineteenth century. J. Geophys. Res., 108(D14), 4407, doi: 10.1029/2002JD002670.

Redi, M.H., 1982: Oceanic isopycanal mixing by coordinate rotation. J. Phys. Oceanogr., 12, 1154-1158.

Rintoul, S.R., and C. Wunsch, 1991. Mass, heat, oxygen and nutrient fluxes and budgets in the North Atlantic Ocean. Deep-Sea Res., 38 (Suppl. 1), S355-S377.

Rintoul, S.R., and S. Sokolov, 2001. Baroclinic transport variability of the Antarctic Circumpolar Current south of Australia (WOCE repeat section SR3). J. Geophys. Res., 106(C2), 2815-2832.

Roberts, M.J., H. Banks, N. Gedney, J. Gregory, R. Hill, S. Mullerwoth, A. Pardaens, G. Pickard, T. Thorpe, and R. Wood, 2004: Impact of an eddy-permitting ocean resolution on control and climate change simulations with a global coupled GCM. J. Climate, 17, 3-20.

Roeckner, E., G. Bäuml, L. Bonaventura, R. Brokopf, M. Esch, M. Giorgetta, S. Hagemann, I. Kirchner, L. Kornblueh, E. Manzini, A. Rhodin, U. Schlese, U. Schulzweida, and A. Tompkins, 2003: The atmospheric general circulation model ECHAM5, part I: Model description. Max- Planck- Institut für Meteorologie, Report No. 349, 127pp.

Ross, C.K., 1984: Temperature-salinity characteristics of the "overflow" water in Denmark Strait during "Overflow '73". Rapp. P.-v. Reun. Cons. Int. Explor. Mer., 185, 111-119.

Saunders, P., 1990: Cold outflow from the Faroe Bank Channel. J. Phys. Oceanogr., 20, 29-43.

Sloyan, B., and S. Rintoul, 2001: The Southern Ocean limb of the global deep overturnng circulation. J. Phys. Oceanogr., 31, 143-173.

Steele, M. , R. Morley, and W. Ermold, 2001: PHC: A global ocean hydrography with high-quality Arctic Ocean. J. Climate, 14, 2079-2087.

Talley, L.D., J.L. Reid, and P.E. Robbins, 2003: Data-based meridional overturning streamfunctions for the global ocean. J. Climate, 16, 3213-3226.

Trenberth, K.E., and A. Solomon, 1994: The global heat balance: Heat transports in the atmosphere and ocean. Climate Dyn., 10, 107-134.

Trenberth, K.E., and J.M. Caron, 2001: Estimates of meridional atmosphere and ocean heat transports. J. Climate, 14, 3433-3443.

VanOldenborgh, G.J., S.Y. Philips, and M. Collins, 2005: El Niño in a changing climate: a multi model study. Ocean Science, 1, 81-95.

Valcke, S., A. Caubel, D. Declat, L. Terray, 2003: OASIS Ocean Atmosphere Sea Ice Soil users's guide. CERFACS Tech. Rep. TR/CMGC/03/69, Toulouse, France, 85pp.

Vialard, J., C. Menkes, J.-P. Boulanger, P. Delecluse, E. Guilyardi, M.J. McPhaden, and G. Madec, 2001: A model study of oceanic mechanisms affecting equatorial Pacific sea surface temperature during the 1997-1998 El Niño. J. Phys. Oceanogr., 31, 1649-1675.

Vinje, T., 2001: Fram Strait ice fluxes and atmospheric circulation: 1950-2000. J. Climate, 14, 3508-3517.

Washington, W.M., J.W. Weatherly, G.A. Meehl, A.J. Semtner Jr., T.W. Bettge, A.P. Craig, W.G. Strand Jr., J. Arblaster, V.B. Wayland, R. James, and Y. Zhang, 2000: Parallel climate model (PCM) control and transient simulations. Climate Dynamics, 16, 755-774.

Weisberg, R.H., 1984: Seasonal adjustments in the equatorial Atlantic during 1983 as seen by surface moorings. Geophys. Res. Lett., 11(8), 733-735.

Weisberg, R. H., and L. Qiao, 2000: Equatorial upwelling in the central Pacific estimated from moored velocity profilers, J. Phys. Oceanogr., 30, 105-124.

Wetzel, P. E. Maier-Reimer, M. Botzet, J. Jungclaus, and N. Keenlyside, 2005: Effects of ocean biology on the penetrative radiation in a coupled climate model, J. Climate (this issue).

Willis, J.K., D. Roemmich, and B. Cornuelle, 2004: Interannual variability in upper ocean heat content, temperature, and thermosteric expansion on global scales. J. Geophys. Res., 109, C12036, doi: 10.1029/2003JC002260.

Wijffels, S. E., R.W. Schmitt, H.L. Bryden, and A. Stigebrandt, 1992: Transport of freshwater by the oceans. J. Phys. Oceanogr., 25, 3186-3195.

Wijffels, S., 2001: Ocean transport of freshwater. Ocean Circulation and Climate, G. Siedler et al., Eds., Academic Press, 475-488.

Wijffels, S., N. Bray, S. Hautala, G. Meyers, and W.M.L. Morawitz, 1996: The WOCE Indonesian throughflow repeat sections: I10 and IR6. International WOCE Newsletter, No. 24, WOCE International Project Office, Southampton, United Kingdom, 25-28.

Wolff, J.O., E. Maier-Reimer, E., Legutke, S., 1997: The Hamburg Ocean Primitive Equation Model HOPE. Technical Report No. 13, German Climate Computer Center (DKRZ), Hamburg, Germany.

Table captions:

Table 1: Statistics for monthly mean anomalies of the Niño 3 index for the year 1953-2002 from the HADISST data, and the last 50 years of the NWSC and WSC experiments, respectively. Time series are detrended and the seasonal cycle removed.

Table 2: Correlation between the main heat budget tendency terms (udT/dt = zonal advection, vdT/dy = meridional advection, wdT/dt = vertical advection, and SFHFL = surface heat fluxes) and the SST tendency (dT/dt).

Figure captions:

Figure 1: Model grid (only every fifth grid line is displayed) and land sea mask. White regions over Greenland and Antarctica denote the grid poles of the curvilinear grid.

Figure 2: Time series of a) global mean SST [˚C], b) SST [˚C]averaged over the Niño-3 region (5S-5N, 150W-90W), c) Northern Hemisphere sea ice area [10^{12} m^2], and d) Southern Hemisphere sea ice area [10^{12} m^2]. The respective data from the HADISST climatology for the years 1980-2003 are shown for comparison to the right of each model time series. Thin lines denote monthly means, thick lines 12 month running means.

Figure 3: a) the model SST averaged over the last 50 years of the simulation (experiment WSC) minus the HADISST climatogical SST [K]. Contour interval (CI) is 1 K; regions where the SST error exceeds 1 K are shaded dark grey, regions where the simulated SST is more than 1 K colder as the observations are shaded light grey; b) the total precipitation field [mm/day] of experiment WSC minus the mean annual precipitation from CMAP (Xie and Arkin, 1997).

Figure 4: Simulated (right) and observed (left) Sea ice concentration in the Northern Hemisphere in late winter (March, upper panels) and late summer (September, lower panels). Observational estimates are taken from the HADISST data sets. CI is 20% starting at 10%. Simulated sea ice velocities (only every fourth vector) are also shown for those areas where the concentration exceeds 50%.

Figure 4 (continued): Simulated (right) and observed (left) Sea ice concentration in the Southern Hemisphere in late summer (March, upper panels) and late winter (September, lower panels). Observational estimates are taken from the HADISST data sets. CI is 20% starting at 10%. Simulated sea ice velocities (only every fourth vector) are also shown for those areas where the concentration exceeds 50%.

Figure 5: Maximum depth [m] of convective overturning [m] during the years 250-300. CI is 500 m.

Figure 6: Mean Atlantic meridional overturning streamfunction averaged over the years 250-300 . CI= 2 Sv [1 Sv= 10^6 m^3s^{-1}], negative values are shaded.

Figure 7: Meridional global (upper) and Atlantic (lower) heat transports (in PW) implied by net ocean to atmosphere heat flux (left column) and meridional global (upper) and Atlantic (lower) fresh water transport (in Sv) implied by the net ocean to atmosphere fresh water flux (right column). The ocean data were averaged over the last 50 years of the simulation. Heat transport estimates with error bars based on observations are taken from Rintoul and Wunsch (1991), Macdonald and Wunsch (1996), and Johns et al. (1997). Estimates derived from the top of the atmosphere as part of the earth radiation budget (ERBE) experiment are taken from

Trenberth and Solomon (1994). Fresh water transport based on direct observations are taken from various sources compiled in Wijffels (2001).

Figure 8: Change in a) wind stress curl [10^{-7} Nm^{-3}], b) surface temperature [K], and c) precipitation [mm/day] between the experiment including the wind stress correction (WSC) and the respective experiment without this parameterization (NWSC). For both experiments the fields were averaged over the model years 250-300. In a), CIs are -0.3,-0.2, 0, 0.2, 0.3 ($\times 10^{-7} Nm^{-3)}$, values exceeding $0.1 \times 10^{-7} Nm^{-3}$ are shaded light grey, values less than –0.1 Nm^{-3} are shaded dark grey; in b) CI is 0.5 K, values exceeding 0.5 K are shaded dark grey, values less than –0.5 K are shaded light grey; in c) CI is 0.5 mm/day but the –0.2 and 0.2 mm/day isolines are displayed instead of the (noisy) zero contours.

Figure 9: a) Mean wind stress (vectors) and magnitude (contours) [Pa] in the experiment WSC, b) changes in wind stress between the experiment WSC and NWSC. Regions, where the magnitude of the wind stress is reduced by more than 0.005 Pa are shaded light gray, regions where the difference exceeds 0.005 Pa are shaded dark gray. c) Changes in ocean upwelling (in m yr^{-1}) at 50m depth. Regions where the upwelling difference exceeds +100 m yr^{-1} are shaded light gray, regions where the difference exceeds –100 myr^{-1} are shaded dark gray.

Figure 10: Tropical Pacific upper ocean (50m) heat budget for the WSC experiment (left column) and the difference in the respective heat budget terms between WSC and NWSC (right column). Temperature tendency (K/month) contributions from (a, b) the surface heat flux forcing, (c, d) horizontal advection, (e, f) vertical advection, and (g, h) the mixing terms.

Figure 11: Power spectra of Niño3 averaged SST anomalies from HADISST observations (dot-dashed), and the last 100 years of the WSC (solid) and NWSC (dashed) experiments.

Figure 12: Annual cycle (K) along the equator (2N-2S), deviations from the annual means for a) the HADISST data, and b) the last 50 years of the model simulation.

Figure 12 c: The standard deviation [K] of Niño3 SST as a function of the calendar month for the HADISST (1953-2002) data (thick line), and for the last 50 years of the WSC experiment (dashed line) and the NWSC experiment (thin solid line).

Figure 13: Correlations between the SST averaged over the Niño-3 region and the global SST for a) the HADISST, and b) the coupled experiment WSC. Regions where the correlations exceeds + or – 0.4 are shaded dark grey or light grey, respectively.

Figure 14: Evolution of SST anomalies (K) along the equator for (left) the HADISST climatology, (middle) the NWSC, and (right) the WSC experiment.

Figure 15: Scatter plot of the Nino3 SST anomalies versus the wind stress anomalies over the western equatorial Pacific for a) the experiment NWSC, and b) the experiment WSC. Anomalies are calculated from model years 78 to 300 after detrending.

Tables

DATA	Std. Dev.	skewness	Kurtosis -3
HADISST	**0.88**	**0.911**	**1.362**
WSC	**1.42**	**0.025**	**0.206**
NWSC	**1.79**	**0.034**	**0.280**

Table 1: Statistics for monthly mean anomalies of the Niño 3 index for the year 1953-2002 from the HADISST data, and the last 50 years of the NWSC and WSC experiments, respectively. Time series are detrended and the seasonal cycle removed.

Experiment	NWSC	WSC
dT/dt	**1**	**1**
udT/dx	**0.182**	**0.063**
vdT/dy	**0.629**	**0.244**
wdT/dz	**0.443**	**0.657**
SFHFL	**0.3083**	**0.2097**

Table 2: Correlation between the main heat budget tendency terms (udT/dt = zonal advection, vdT/dy = meridional advection, wdT/dt = vertical advection, and SFHFL = surface heat fluxes) and the SST tendency (dT/dt).

Figures

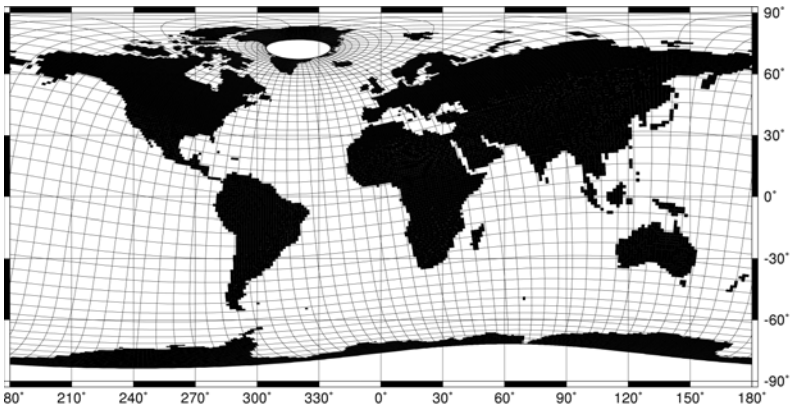

Figure 1: Model grid (only every fifth grid line is displayed) and land sea mask. White regions over Greenland and Antarctica denote the grid poles of the curvilinear grid.

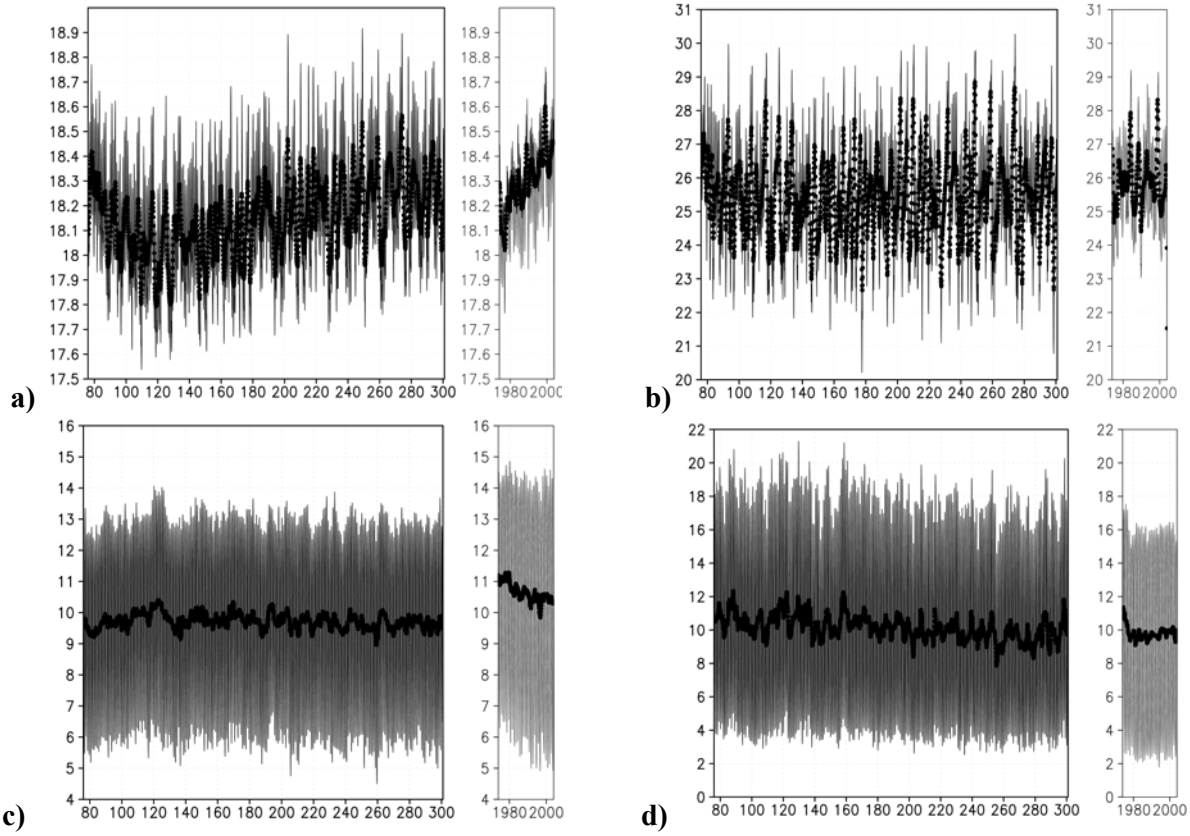

Figure 2: Time series of a) global mean SST [˚C], b) SST [˚C]averaged over the Niño-3 region (5S-5N, 150W-90W), c) Northern Hemisphere sea ice area [10^{12} m^2], and d) Southern Hemisphere sea ice area [10^{12} m^2]. The respective data from the HADISST climatology for the years 1980-2003 are shown for comparison to the right of each model time series. Thin lines denote monthly means, thick lines 12 month running means.

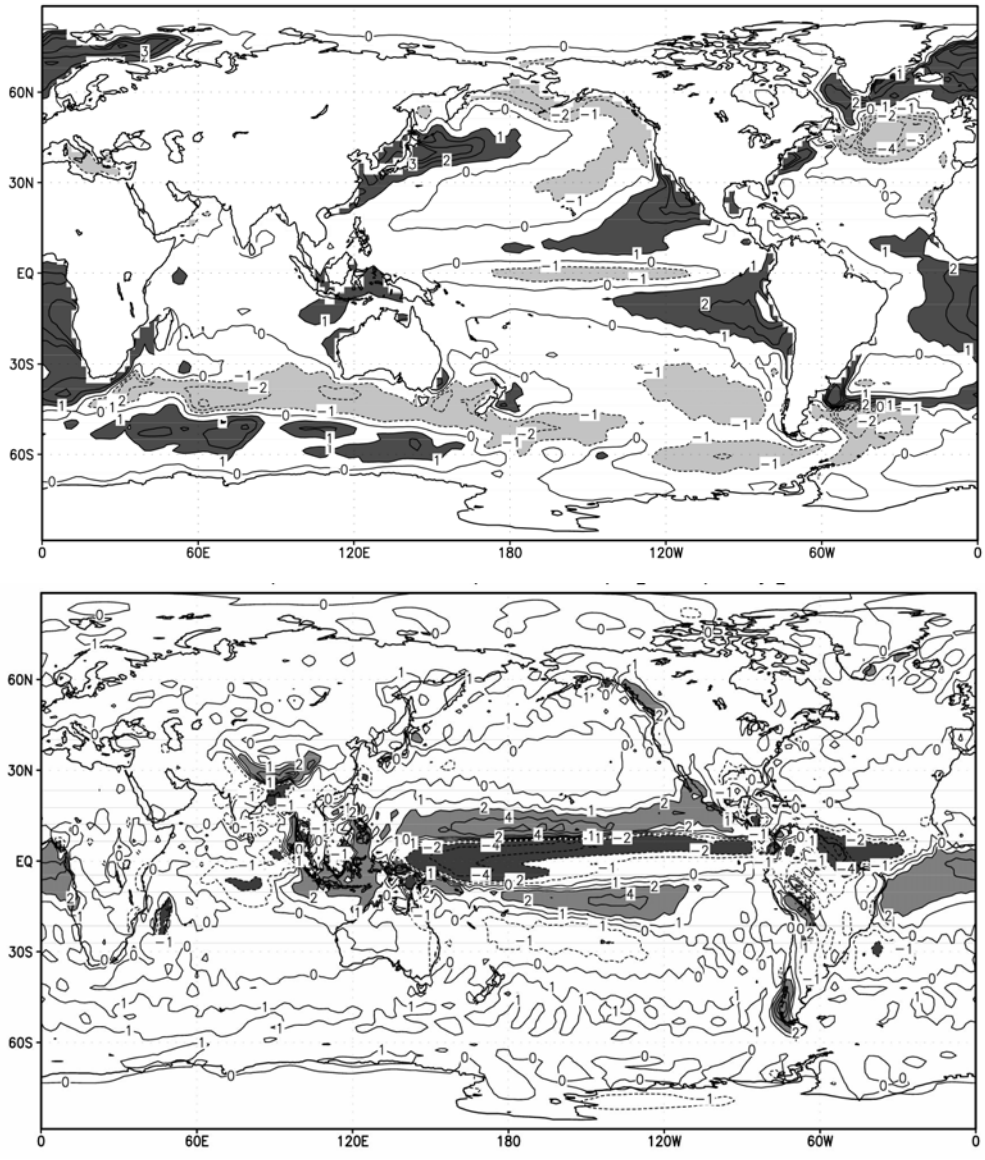

a)

b)

Figure 3: a) the model SST averaged over the last 50 years of the simulation (experiment WSC) minus the HADISST climatogical SST [K]. Contour interval (CI) is 1 K; regions where the SST error exceeds 1 K are shaded dark grey, regions where the simulated SST is more than 1 K colder as the observations are shaded light grey; b) the total precipitation field [mm/day] of experiment WSC minus the mean annual precipitation from CMAP (Xie and Arkin, 1997).

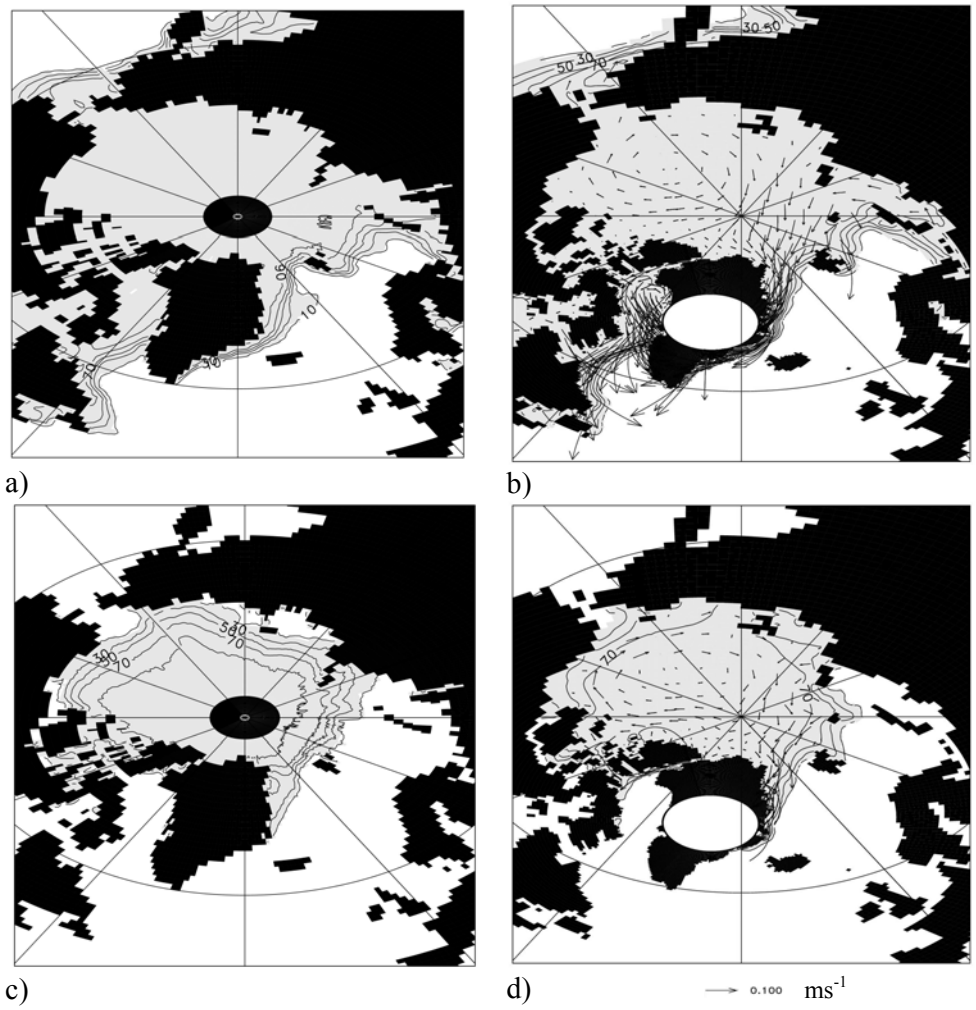

Figure 4: Simulated (right) and observed (left) Sea ice concentration in the Northern Hemisphere in late winter (March, upper panels) and late summer (September, lower panels). Observational estimates are taken from the HADISST data sets. CI is 20% starting at 10%. Simulated sea ice velocities (only every fourth vector) are also shown for those areas where the concentration exceeds 50%.

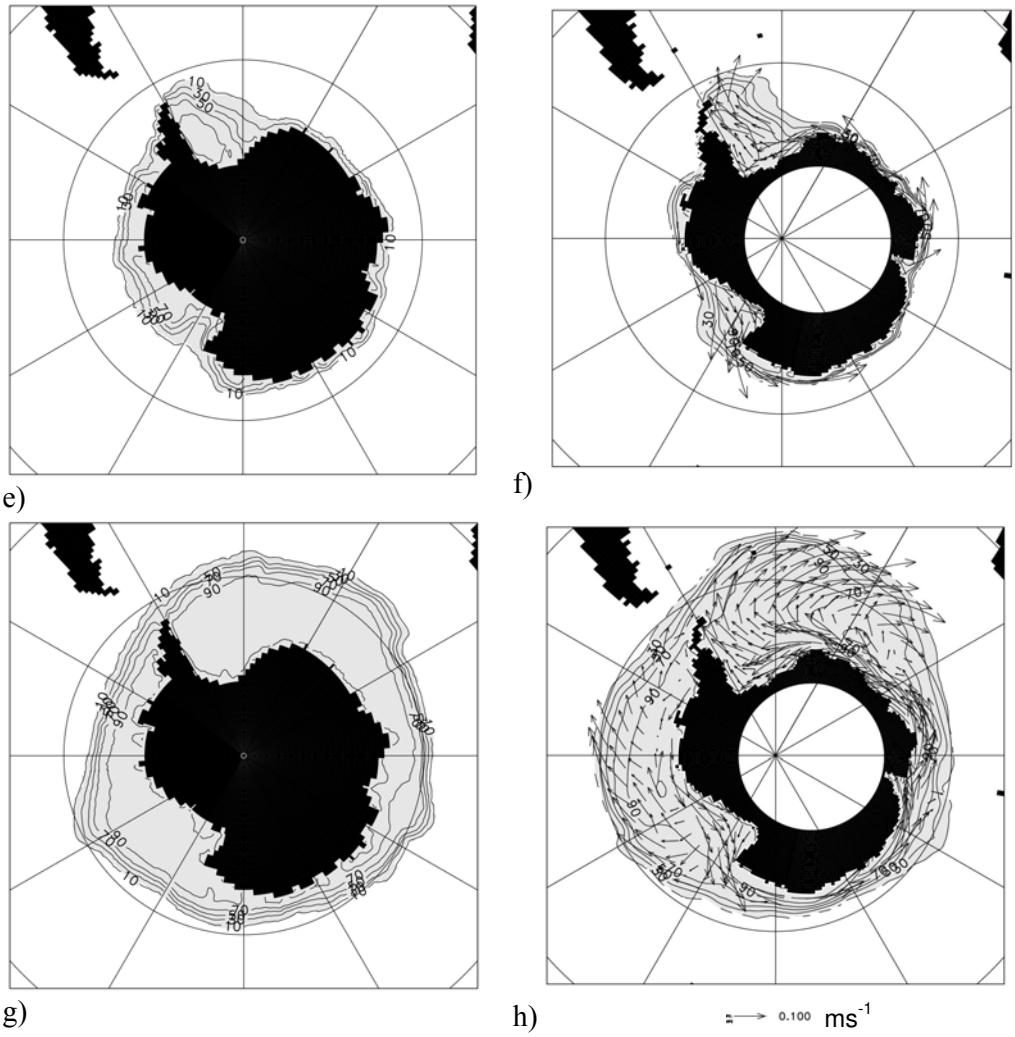

Figure 4 (continued): Simulated (right) and observed (left) Sea ice concentration in the Southern Hemisphere in late summer (March, upper panels) and late winter (September, lower panels). Observational estimates are taken from the HADISST data sets. CI is 20% starting at 10%. Simulated sea ice velocities (only every fourth vector) are also shown for those areas where the concentration exceeds 50%.

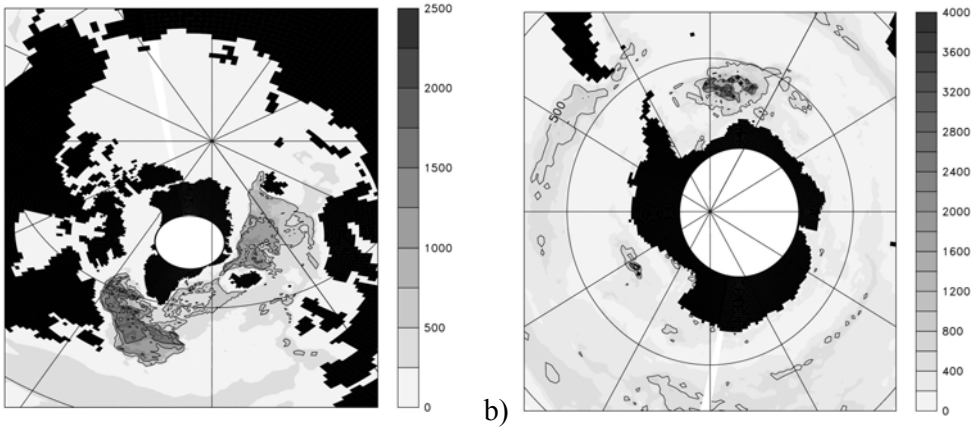

Figure 5: Maximum depth [m] of convective overturning [m] during the years 250-300. CI is 500 m.

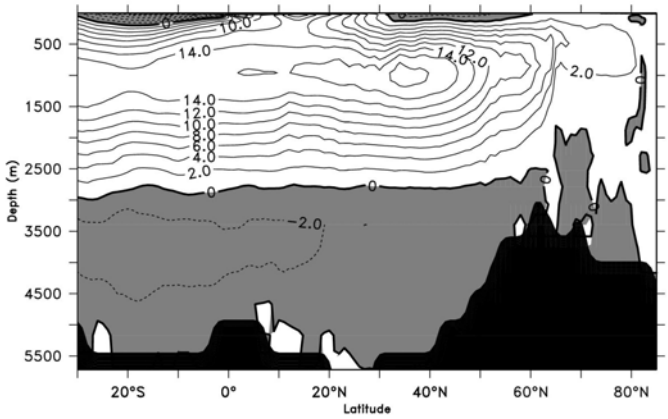

Figure 6: Mean Atlantic meridional overturning streamfunction averaged over the years 250-300 . CI= 2 Sv [1 Sv= 10^6 m^3s^{-1}], negative values are shaded.

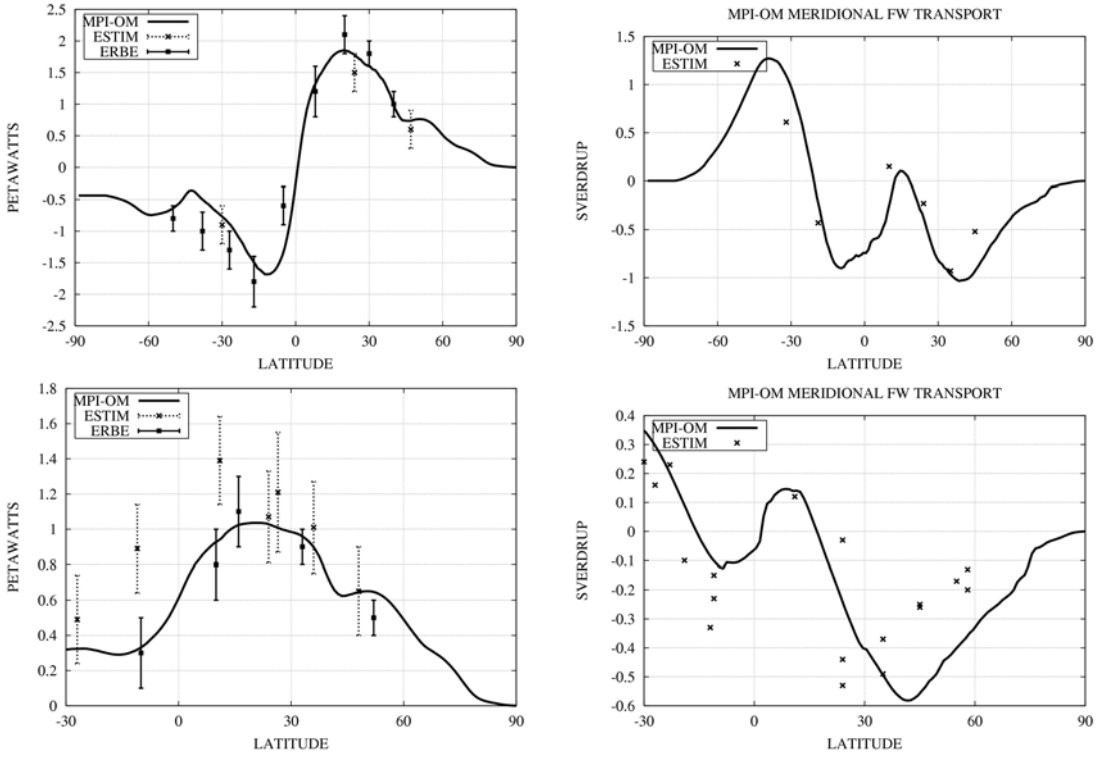

Figure 7: Meridional global (upper) and Atlantic (lower) heat transports (in PW) implied by net ocean to atmosphere heat flux (left column) and meridional global (upper) and Atlantic (lower) fresh water transport (in Sv) implied by the net ocean to atmosphere fresh water flux (right column). The ocean data were averaged over the last 50 years of the simulation. Heat transport estimates with error bars based on observations are taken from Rintoul and Wunsch (1991), Macdonald and Wunsch (1996), and Johns et al. (1997). Estimates derived from the top of the atmosphere as part of the earth radiation budget (ERBE) experiment are taken from Trenberth and Solomon (1994). Fresh water transport based on direct observations are taken from various sources compiled in Wijffels (2001).

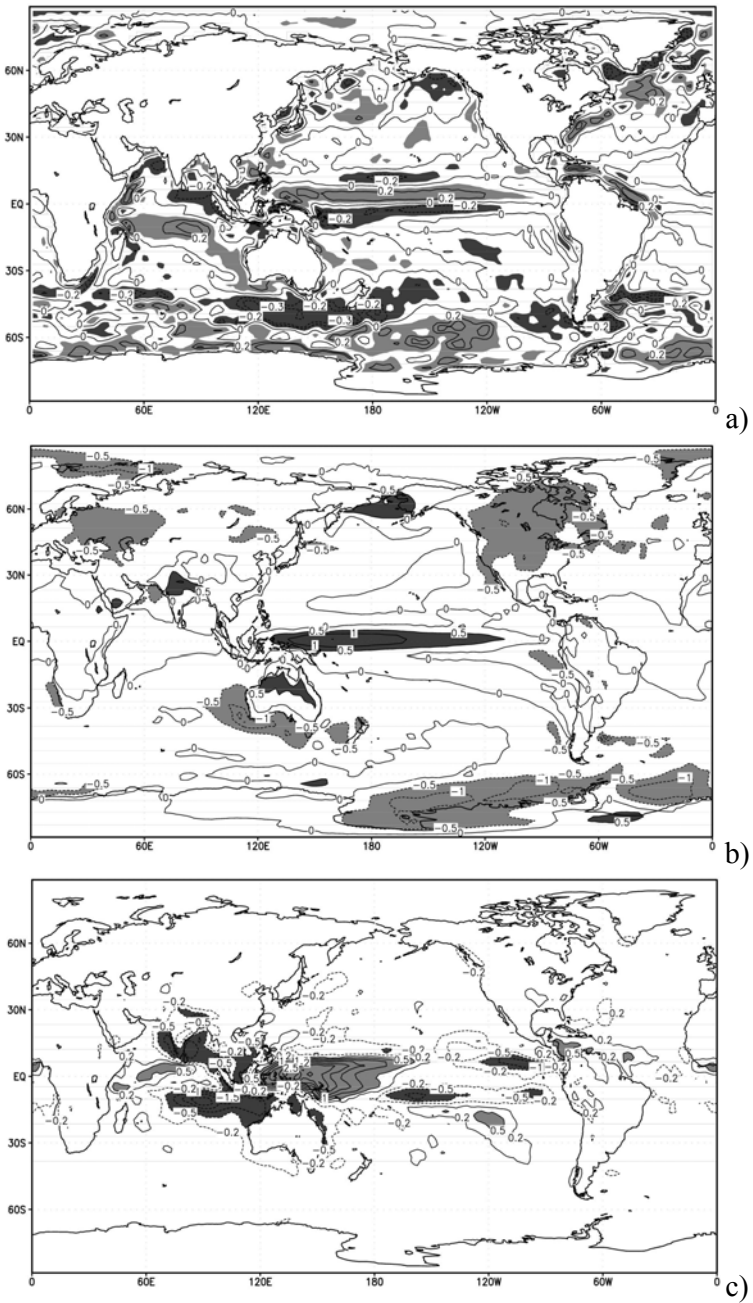

Figure 8: Change in a) wind stress curl [10^{-7} Nm^{-3}], b) surface temperature [K], and c) precipitation [mm/day] between the experiment including the wind stress correction (WSC) and the respective experiment without this parameterization (NWSC). For both experiments the fields were averaged over the model years 250-300. In a), CIs are –0.3,-0.2, 0, 0.2, 0.3 ($\times 10^{-7} Nm^{-3}$), values exceeding $0.1 \times 10^{-7} Nm^{-3}$ are shaded light grey, values less than –0.1 Nm^{-3} are shaded dark grey; in b) CI is 0.5 K, values exceeding 0.5 K are shaded dark grey, values less than –0.5 K are shaded light grey; in c) CI is 0.5 mm/day but the –0.2 and 0.2 mm/day isolines are displayed instead of the (noisy) zero contours.

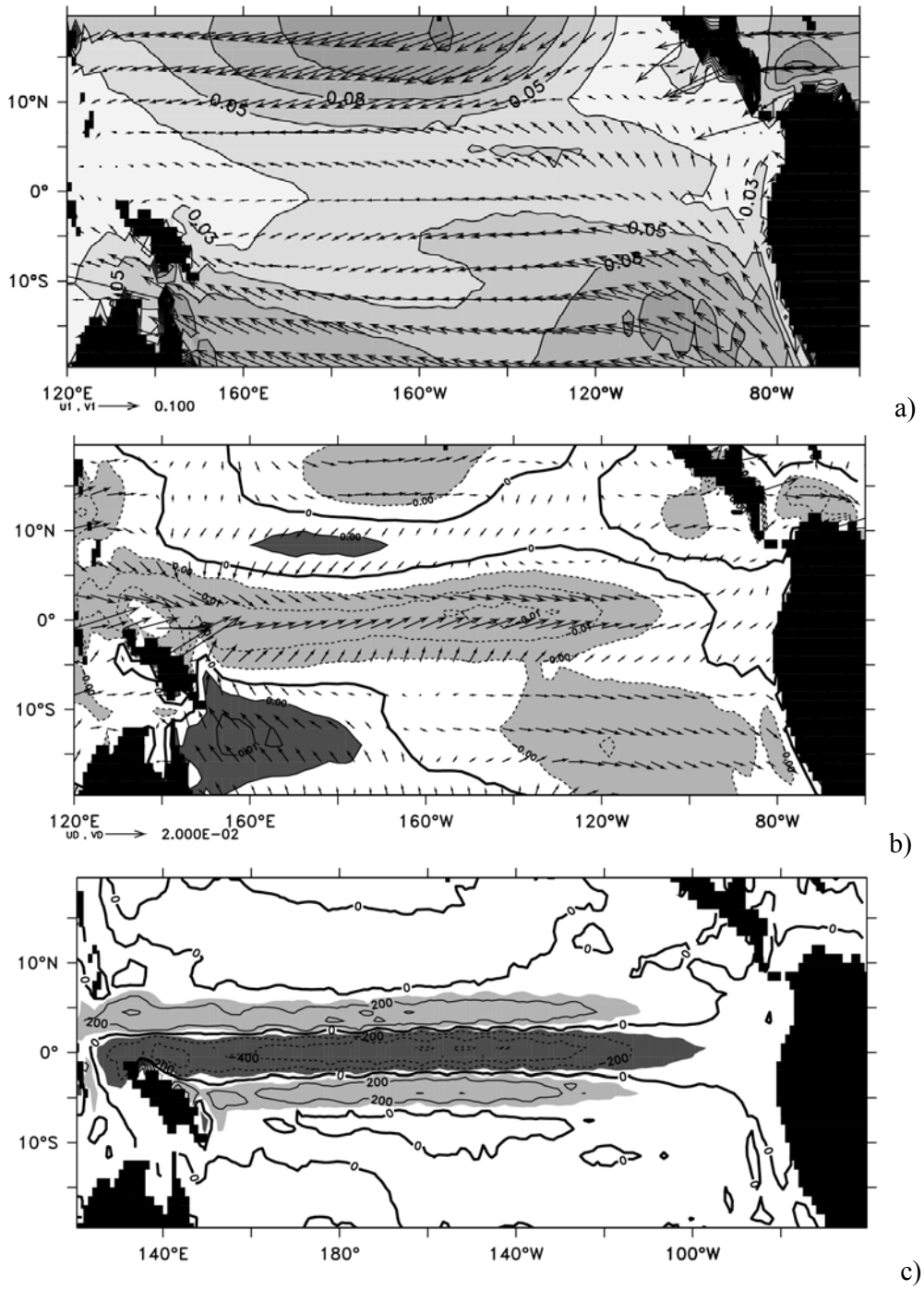

Figure 9: a) Mean wind stress (vectors) and magnitude (contours) [Pa] in the experiment WSC, b) changes in wind stress between the experiment WSC and NWSC. Regions, where the magnitude of the wind stress is reduced by more than 0.005 Pa are shaded light gray, regions where the difference exceeds 0.005 Pa are shaded dark gray. c) Changes in ocean upwelling (in m yr^{-1}) at 50m depth. Regions where the upwelling difference exceeds +100 m yr^{-1} are shaded light gray, regions where the difference exceeds –100 myr^{-1} are shaded dark gray.

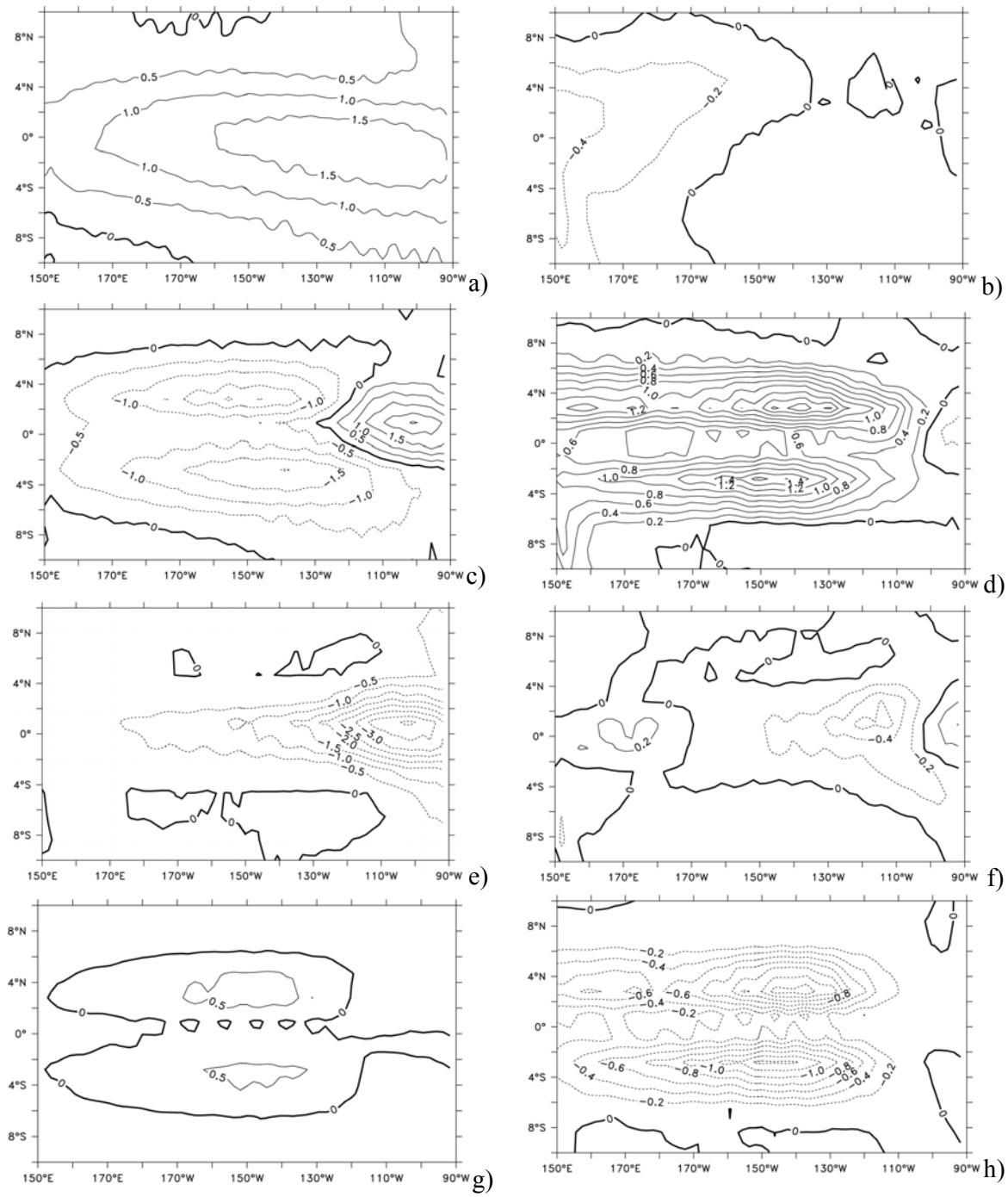

Figure 10: Tropical Pacific upper ocean (50m) heat budget for the WSC experiment (left column) and the difference in the respective heat budget terms between WSC and NWSC (right column). Temperature tendency (K/month) contributions from (a, b) the surface heat flux forcing, (c, d) horizontal advection, (e, f) vertical advection, and (g, h) the mixing terms.

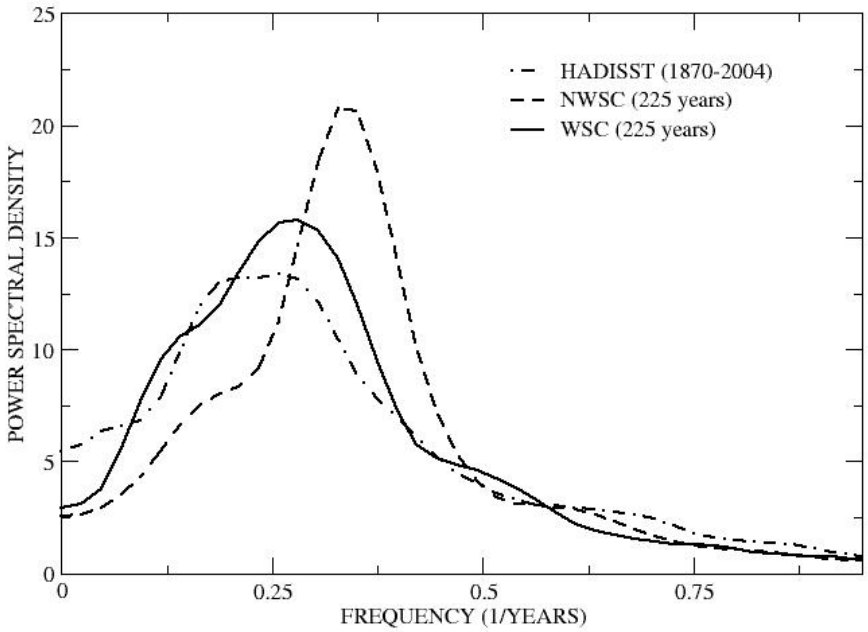

Figure 11: Power spectra of Niño3 averaged SST anomalies from HADISST observations (dot-dashed), and the last 100 years of the WSC (solid) and NWSC (dashed) experiments.

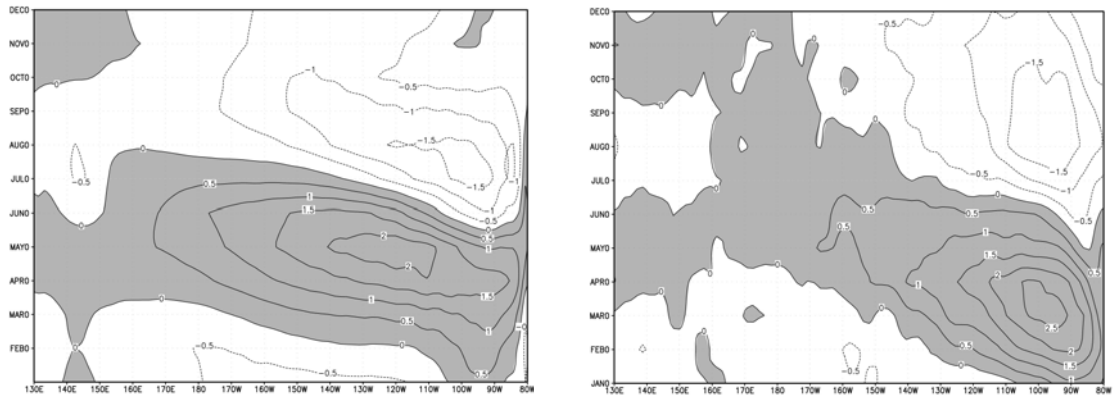

a) b)

Figure 12: Annual cycle (K) along the equator (2N-2S), deviations from the annual means for a) the HADISST data, and b) the last 50 years of the model simulation.

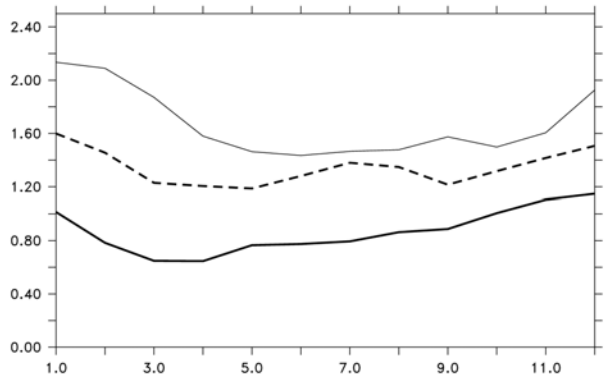

Figure 12 c: The standard deviation [K] of Niño3 SST as a function of the calendar month for the HADISST (1953-2002) data (thick line), and for the last 50 years of the WSC experiment (dashed line) and the NWSC experiment (thin solid line).

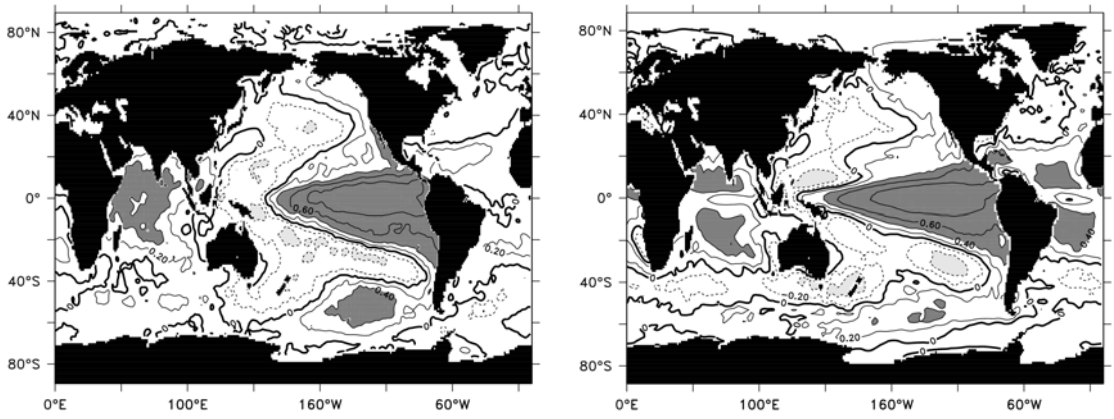

a) **b)**

Figure 13: Correlations between the SST averaged over the Niño-3 region and the global SST for a) the HADISST, and b) the coupled experiment WSC. Regions where the correlations exceeds + or – 0.4 are shaded dark grey or light grey, respectively.

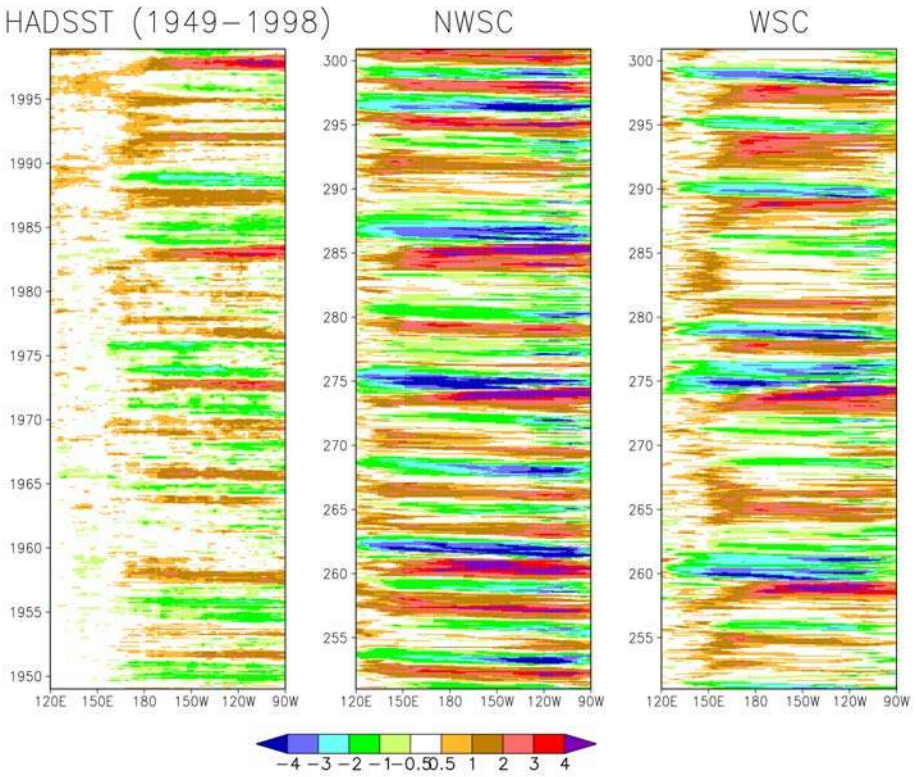

Figure 14: Evolution of SST anomalies (K) along the equator for (left) the HADISST climatology, (middle) the NWSC, and (right) the WSC experiment.

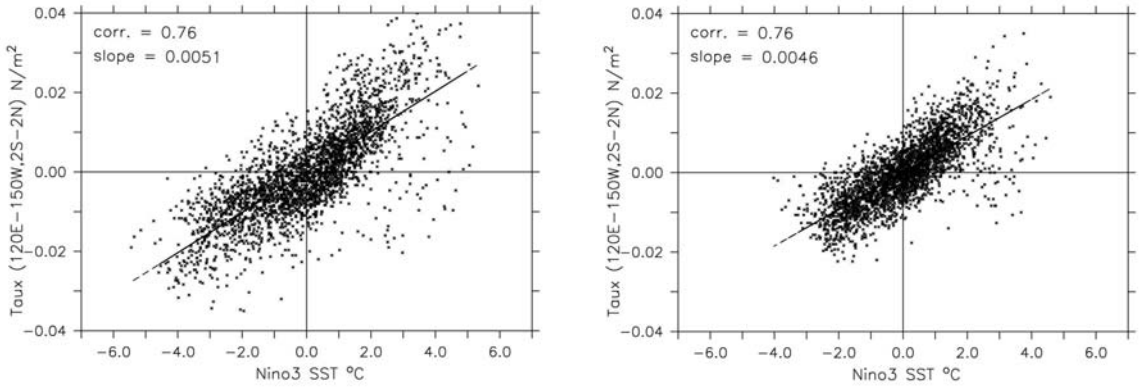

Figure 15: Scatter plot of the Nino3 SST anomalies versus the wind stress anomalies over the western equatorial Pacific for a) the experiment NWSC, and b) the experiment WSC. Anomalies are calculated from model years 78 to 300 after detrending.